
MOX–Report No. 46/2014

# The role of the microvascular tortuosity in tumor transport phenomena

Penta, R; Ambrosi, D.

MOX, Dipartimento di Matematica "F. Brioschi"
Politecnico di Milano, Via Bonardi 9 - 20133 Milano (Italy)

mox@mate.polimi.it http://mox.polimi.it

# The role of the microvascular tortuosity in tumor transport phenomena

R.Penta[a,b], D.Ambrosi[a,*]

[a]*MOX, Dipartimento di Matematica, Politecnico di Milano, Piazza Leonardo da Vinci 32, 20133, Milano, Italy*
[b]*Technische Universität Darmstadt, Fachbereich Mathematik, Numerik und Wissenschaftliches Rechnen, Dolivostr. 15, 64293, Darmstadt, Germany (present address)*

**Abstract**

The role of the microvascular network geometry on transport phenomena in solid tumors and its interplay with the leakage and pressure drop across the vessels is qualitatively and quantitatively discussed. Our starting point is a multiscale homogenization, suggested by the sharp length scale separation that exists between the characteristic vessels and tumor tissue spatial scales, referred to as the *microscale* and the *macroscale*, respectively. The coupling between interstitial and capillary compartment is described by a double Darcy model on the macroscale, whereas the geometric information on the microvascular structure is encoded in the effective hydraulic conductivities, which are numerically computed solving classical differential problems on the microscale representative *cell*. Then, microscale information is injected into the macroscopic model, which is analytically solved in a prototypical geometry and compared with previous experimentally validated, phenomenological models. In this way, we are able to capture the role of the standard blood flow determinants in the tumor, such as the tumor radius, tissue hydraulic conductivity and vessels permeability, as well as the influence of the vascular *tortuosity* on fluid convection. The results quantitatively confirm that transport of blood (and, as a consequence, of any advected anti-cancer drug) can be dramatically impaired by increasing the geometrical complexity of the microvasculature. Hence, our quantitative analysis supports the argument that geometric regularization of the capillary network improve blood transport and drug delivery in the tumor mass.

*Keywords:* Multiscale Homogenization, Blood Transport, Tumor Microvasculature, Anti-cancer therapies

## 1. Introduction

The bio-physical mechanisms that drive solute and blood transport through a vascularized tissue have inspired a large literature in the last decades, both from an experimental and from a mathematical modelling viewpoint. The clinical motivations can reside in the optimization of oxygen transport in surgical tissue transfer (Matzavinos et al., 2009) or in the in the determination of the main factors in vascular arrangement (Ambrosi et al., 2004). Several mathematical and numerical techniques have been adopted to explore the behavior of a system where the relatively small number of involved cells makes a cellular automata approach attractive (Alarcón et al., 2003; Powathil et al., 2012). Here we focus on malignant vascular networks and on the specific geometrical and hydraulic properties of this network. The ability of an injected anti-cancer or tracker molecule to reach the target cancer cells depends on several key mechanisms which can be regarded as transport *barriers*: advection in the blood vessels, leakage from the microvascular walls, transport in the interstitial space and interactions with the tumor cells membrane (Jain, 1987). Experimental measurements, as well as validated mathematical models which highlight the determinants of tumor blood convection, can therefore play a role in the improvement of anti-cancer therapies.

The tumor system is characterized by several abnormal features, including a leaking and tortuous microvascular network (Hashizume, 2000), the lack of a functional lymphatic drainage, elevated and heterogeneous interstitial pressure through the tumor volume. Jain and Baxter (1988) developed a phenomenological mathematical model to describe the blood transport in the tumor mass. The authors considered an isotropic spherical solid tumor, where

*Corresponding author
*Email addresses:* penta@mathematik.tu-darmstadt.de (R.Penta), davide.ambrosi@polimi.it (D.Ambrosi )

the blood leakage through the vessels is modeled as an effective source for the interstitial Darcian fluid. As a result, they can track significant spatial variations in the interstitial pressure profile, which rapidly increases from the tumor boundary to the center, so that the pressure difference between blood vessels and tumor interstitium decreases accordingly. The blood convection is improved (i.e. the interstitial pressure is damped) by decreasing the tumor radius, the vascular hydraulic conductivity and the exchange surface-to-volume ratio as well as increasing the tumor hydraulic conductivity. The model by Jain and Baxter (1988) has been experimentally validated in Boucher et al. (1990), while the role of the revelant measured blood flow determinants, as well as a discussion regarding recently developed normalization therapies, is highlighted in Jain et al. (2007).

In this work, we start from the multiscale double Darcy model developed by Shipley and Chapman (2010) for interstitial and capillary fluid transport, which is derived exploiting the sharp length scale separation between the intercapillary distance and the tumor characteristic dimensions. The model accounts for both the interstitial and blood vessels flow and the effective hydraulic conductivities are computed numerically solving the classical Laplace and Stokes' problem in a reference prototypical cell. We numerically solve the isotropic tissue scale model for several cell geometries in order to capture the tortuosity impact on blood convection in the tumor mass. The model formally resembles Jain and Baxter (1988), but spatial variations of the microvascular pressure are now allowed and new parameters which describe the capillary network hydraulic properties arise. For increasing vascular tortuosity, we predict a dramatic capillary hydraulic conductivity damp which highly compromises the fluid flow within the tumor. The novel contribution of this work is the qualitative and quantitative evaluation of the vascular geometric complexity on the blood transport process. On the basis of our analysis, we suggest that anti-cancer therapies related to a blood flow improvement should focus on geometric vessels regularization.
The work is organized as follows:

- In Section 2 we introduce the multiscale homogenized model by Shipley and Chapman (2010), which is starting point of the present analysis.
- In section 3 we present and discuss the 3D numerical solution of the capillary and interstitial microscale cell problems for the macroscale isotropic setting.
- In section 4 we present and discuss the macroscopic model solution and the impact of the microvascular tortuosity on tumor blood convection is pointed out.
- In section 5 we compare our results with those obtained by Jain and Baxter (1988) and discuss the role of the key blood flow determinants.
- In section 6 we apply our results to a sample drug transport problem.
- In secton 7 concluding remarks are presented.

## 2. Mathematical Model

In a recent paper Shipley and Chapman (2010) derive a mathematical model to describe the fluid dynamics in a vascularized tumor at the tissue scale, on the basis of the multiscale homogenization technique (Sanchez-Palencia, 1983; Holmes, 1995; Mei and Vernescu, 2010). They define the interstitial and capillary phases as two individual compartments on the microscale, where Darcy and Stokes regimes apply, respectively. The coupling between the two compartments is provided by continuity of the blood flux, which is prescribed by means of the Starling's law, i.e. it is assumed proportional to the fluid pressure drop across the vessels walls. Then, the multiple scales technique is exploited, under assumption of local periodicity, to derive a double Darcy model. The geometric information on the microvasculature turns out to be encoded in the hydraulic conductivity tensors, which are to be computed solving classical microscale differential problems on the representative periodic cell. The final set of equations comprises effective mass sources, accounting for the blood leakage on the macroscale, and the macroscopic fluid dynamics of both the tumor interstitium and the capillary network. The crucial assumption underneath the homogenization technique is the sharp length scale separation between the local scale, where distinct microscopic features of the physical system can be identified, and the macroscale, where only global variations of the relevant field of interest can be captured, as shown in Figure 1.

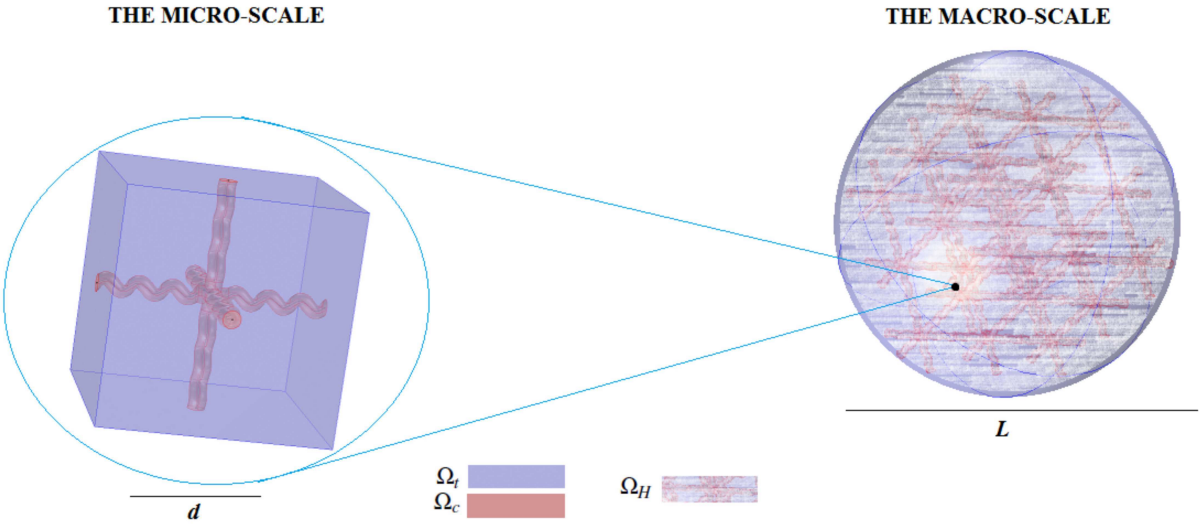


Figure 1: A schematic representation of the micro and macro scales. On the left hand side, the microscale cell $\Omega$ is shown and the difference between the interstitial and capillary compartment $\Omega_t$ and $\Omega_c$ is pointed out. On the right hand side, the homogenized domain $\Omega_H$, where the microstructure is smoothed out, is shown.

| Parameter | Description | Value | Physiological range (Reference) | Value in S.I. units |
|---|---|---|---|---|
| $L_p$ [cm/(mm Hg $\cdot$ s)] | Normalized Vessel hydraulic permeability | $2.38 \cdot 10^{-7}$ | $3.6 \cdot 10^{-8} - 1.8 \cdot 10^{-6}$ (Jain et al., 2007) | $1.79 \cdot 10^{-11}$ [m/(Pa $\cdot$ s)] |
| $\kappa$ [cm$^2$/(mm Hg $\cdot$ s)] | Tumor hydraulic conductivity | $2.8 \cdot 10^{-7}$ | $1.7 - 3.2 \cdot 10^{-7}$ (Boucher et al., 1998) | $2.10 \cdot 10^{-13}$ [m$^2$/(Pa $\cdot$ s)] |
| $\mu$ [Pa $\cdot$ s] | Blood viscosity | $4.0 \cdot 10^{-3}$ | $4.0 \cdot 10^{-3}$ (Rand et al., 1964) | $4 \cdot 10^{-3}$ [Pa $\cdot$ s] |
| $q$ [Dimensionless] | Slip coefficient | 1 | 1 (Shipley and Chapman, 2010) | |
| $r_c$ [Dimensionless] | Capillary radius | 0.07 | | |
| $l$ [Dimensionless] | One-side branch length | 0.8 | | |
| $h$ [Dimensionless] | Cylindrical link height | 0.24 | | |
| $l_c$ [Dimensionless] | Total branch length $(2l+h)$ | 1.84 | | |
| $\lvert\Omega\rvert$ [Dimensionless] | Cell volume $((2l+h)^3)$ | 6.23 | | |
| $R$ [Dimensionless] | Tumor radius | 0.5 | | |
| $d$ [$\mu$m] | Reference micro-scale | 40 | | $4 \cdot 10^{-5}$[m] |
| $L$ [cm] | Reference macro-scale | 1 | | $10^{-2}$[m] |
| $i.c.d.$ [$\mu$m] | Intercapillary distance $((2l+h) \cdot d)$ | 73.6 | 61.9 – 93.7 (Yoshii and Sugiyama, 1988) | $7.36 \cdot 10^{-5}$[m] |
| S/V [cm$^{-1}$] | Surface-to-volume ratio $(S/\lvert\Omega\rvert \cdot d^{-1})$ | 92.3 – 130.4 | 50 – 250 (Jain et al., 2007) | $9.23 - 13.04 \cdot 10^3$[m$^{-1}$] |
| D [$\mu$m] | Capillary diameter $(2r_c \cdot d)$ | 5.6 | 4.4 – 15 (Asaishi et al., 1981) | $5.6 \cdot 10^{-6}$[m] |
| R [cm] | Tumor radius $(RL)$ | 0.5 | 0.5 – 2.2 (Hahnfeldt et al., 1999) | $5 \cdot 10^{-3}$[m] |
| $\alpha_J$ [Dimensionless] | $\mathrm{R}\sqrt{\frac{L_p \mathrm{S}}{\kappa \mathrm{V}}}$ | | 3.5 – 17 (Jain et al., 2007) | |
| $D_g$ [cm$^2$/s] | Diffusion coefficient | $1 \cdot 10^{-7}$ | $1.9 \cdot 10^{-8} - 1.87 \cdot 10^{-6}$ (Shipley and Chapman, 2010) | $1 \cdot 10^{-11}$[m$^2$/s] |
| $r$ [cm/s] | Vessels walls permeability | $1.7 \cdot 10^{-5}$ | $1.4 \cdot 10^{-4} - 2.5 \cdot 10^{-5}$ (Modok et al., 2006, 2007) | $1.7 \cdot 10^{-7}$[m/s] |
| $U$ [$\mu$m/s] | Characteristic capillary velocity | 200 | (Shipley and Chapman, 2010) | $2 \cdot 10^{-4}$[m/s] |
| $\mathrm{P}_V$ [mm Hg] | Microvasculature pressure | 20 | 5.5-34 (Jain et al., 2007) | $2.66 \cdot 10^3$[Pa] |
| $\tau_p$ [h] | Plasma clearance time constant | 6 | 3-103.8 (Jain and Baxter, 1988) | $2.16 \cdot 10^4$[s] |
| $\bar{p}$ [Dimensionless] | Microvasculature pressure $\left(\frac{\mathrm{P}_V d^2}{\mu L U}\right)$ | 532 | 143.6 – 904.4 | |
| $\tau$ [Dimensionless] | Plasma clearance time constant $\left(\frac{\tau_p U}{L}\right)$ | 432 | 216 – 7473.6 | |
| T [h] | Time period | 96 | | $3.456 \cdot 10^5$[s] |
| $T$ [Dimensionless] | Time period $\left(\frac{\mathrm{T}U}{L}\right)$ | 6192 | | |

Table 1: Parameters values exploited for analytical analysis and numerical computing. We set non-dimensional microscale and macroscale parameters such that, once the representative lengths are chosen, their dimensional counterparts values belong to the physiological range reported in the literature. We enforced the characteristic time scale $\frac{L}{U}$ and pressure $\frac{\mu L U}{d^2}$ exploited in Shipley and Chapman (2010) to obtain the corresponding non-dimensional quantities.

Following Shipley and Chapman (2010), we relate the characteristic local scale $d$ to the intercapillary distance among vessels, whereas we identify the macroscale with a representative average tumor length $L$. Their ratio is

$$\varepsilon = \frac{d}{L} \ll 1 \tag{1}$$

so that we can define two independent spatial variables $\mathbf{x}$ and $\mathbf{y}$,

$$\mathbf{y} = \frac{\mathbf{x}}{\varepsilon}, \tag{2}$$

spanning the *macro* and *micro* scale, respectively. Since $\mathbf{y}$-periodicity applies on the microscale, the domain $\Omega$ is a single cell, which is composed by the interstitial compartment $\Omega_t$, the capillary compartment $\Omega_c$ and the interface $\Gamma = \partial\Omega_t \cap \partial\Omega_c$.

In this paper we assume periodicity in $\mathbf{y}$ of the fields in the representative cell, which is supposed to be the same in every $\mathbf{x}$, as it is frequently done in multiscale homogenization (examples of generalization in the context of the multiple scales technique can be found, for example, in Burridge and Keller (1981); Penta et al. (2014b)) . This assumption does not strictly apply to a vascular network, which has a tree–like rather than a periodic structure, therefore, it should be relaxed (see, e.g. Penta et al. (2014a)). However, the hierarchy in size that is apparent in healthy capillary networks can be more difficult to identify (or even completely fail) in a malignant tissue . Hence, we do not consider extra terms that would arise in absence of periodicity and, for the sake of simplicity, we focus on a single representative cell as a first step towards gaining a better understanding on the blood transport problem in vascularized tumors.

This analysis focuses on the impact of the geometric properties of the capillary network on blood convection in tumors. We adopt the same modelling assumptions as Shipley and Chapman (2010), i.e. the blood flow phase is Newtonian, the osmotic pressure due to possible differences in drug concentration is neglected and macroscopic variations of the microstructure are ignored. At this stage the classical steps of multiscale homogenization are performed: representation of every field in terms of two independent spatial varibles (also referred to as the "slow" and the "fast" one in the literature), series expansion of the solution in terms of the small parameter $\varepsilon$, determination of a macroscale equation for every zeroth order component, which rigorously represents the homogenized solution for vanishing $\varepsilon$. Thus, denoting the homogenized domain by $\Omega_H \subset \mathbb{R}^3$ , the non-dimensional governing macroscale system of partial differential equations which describes the fluid-dynamics of a vascularized tumor for every $\mathbf{x} \in \Omega_H$ reads:

$$\begin{cases} \nabla_{\mathbf{x}} \cdot (\mathsf{K}\nabla_{\mathbf{x}} p_c) = \dfrac{S}{|\Omega_c|}\bar{L}_p(p_c - p_t) \qquad \text{in } \Omega_H & (3) \\ \nabla_{\mathbf{x}} \cdot (\bar{\kappa}\mathsf{E}\nabla_{\mathbf{x}} p_t) = -\dfrac{S}{|\Omega_t|}\bar{L}_p(p_c - p_t) \qquad \text{in } \Omega_H & (4) \\ \mathbf{u}_c = -\mathsf{K}\nabla_{\mathbf{x}} p_c & (5) \\ \mathbf{u}_t = -\bar{\kappa}\mathsf{E}\nabla_{\mathbf{x}} p_t, & (6) \end{cases}$$

where $p_c$, $p_t$ are the zeroth order macroscopic capillary and interstitial pressure fields, respectively, and $\mathbf{u}_c$, $\mathbf{u}_t$ are the corresponding zeroth order average Darcy velocities, which describe the tissue scale fluid flow. The non-dimensional numbers $\bar{L}_p$ and $\bar{\kappa}$ are defined by:

$$\bar{L}_p = \frac{L_p \mu L^2}{d^3}; \quad \bar{\kappa} = \frac{\kappa\mu}{d^2}, \tag{7}$$

where $L_p$ and $\kappa$ are the physiological vascular hydraulic permeability and tumor hydraulic conductivity, respectively (see Table 1). The cell exchange surface $S$ and subvolumes size $|\Omega_t|$ and $|\Omega_c|$ are

$$|\Omega_m| = \int_{\Omega_m} \mathrm{d}\mathbf{y} \qquad m = t, c, \quad S = \int_{\Gamma} \mathrm{dS}_y. \tag{8}$$

The tensors $\mathsf{K}$ and $\bar{\kappa}\mathsf{E}$ play the role of effective capillary and interstitial hydraulic conductivity and they are defined by:

$$\mathsf{K} = \langle W \rangle_c, \quad \mathsf{E} = \mathsf{I} - \left\langle (\nabla_{\mathbf{y}} \mathbf{P}^t)^{\mathsf{T}} \right\rangle_t, \tag{9}$$

where the brackets $\langle \bullet \rangle_m$ denote the cell integral average operator

$$\langle \bullet \rangle_m = \frac{1}{|\Omega_m|} \int_{\Omega_m} \bullet \, \mathrm{d}\mathbf{y} \qquad m = t, c. \tag{10}$$

The auxiliary tensor $\mathsf{W}(\mathbf{y})$ and vector $\mathbf{P}^t(\mathbf{y})$ satisfy the following *cell* problems:

$$\begin{cases} \nabla^2_{\mathbf{y}} \mathsf{W}^{\mathsf{T}} - \nabla_{\mathbf{y}} \mathbf{P}^c + \mathsf{I} = 0 \quad \text{in } \Omega_c & (11) \\ \nabla_{\mathbf{y}} \cdot \mathsf{W}^{\mathsf{T}} = 0 \quad \text{in } \Omega_c & (12) \\ \mathsf{W}^{\mathsf{T}} \mathbf{n} = 0 \quad \text{on } \Gamma & (13) \\ \mathsf{W}^{\mathsf{T}} \tau = -\phi [(\nabla_{\mathbf{y}} \mathsf{W}^{\mathsf{T}}) \mathbf{n}] \tau \quad \text{on } \Gamma, & (14) \end{cases}$$

$$\begin{cases} \nabla^2_{\mathbf{y}} \mathbf{P}^t = 0 \quad \text{in } \Omega_t & (15) \\ (\nabla_{\mathbf{y}} \mathbf{P}^t) \mathbf{n} = \mathbf{n} \quad \text{on } \Gamma, & (16) \end{cases}$$

where $\mathbf{n}$ represents the outward unit vector normal to the interface, pointing out of the capillary region and into the tissue region, and $\tau$ is any vector tangent to $\Gamma$.
Suitable uniqueness conditions for the auxiliary vectors $\mathbf{P}^t$ and $\mathbf{P}^c$ are to be enforced. For example

$$\langle \mathbf{P}^c \rangle_c = \mathbf{0} \quad \text{in } \Omega_c \quad \text{and} \quad \langle \mathbf{P}^t \rangle_t = \mathbf{0} \quad \text{in } \Omega_t.$$

Exploiting the $\mathbf{y}$-periodicity, the problems for $(\mathsf{W}(\mathbf{y}), \mathbf{P}^c(\mathbf{y}))$ and $\mathbf{P}^t(\mathbf{y})$ are then closed by periodic conditions on the cell boundaries $\partial\Omega_c \setminus \Gamma$ and $\partial\Omega_t \setminus \Gamma$, respectively. The differential problem (15-16) is an inhomogeneous Laplace problem for each component of the vector $\mathbf{P}^t$, whereas (11-14) is a Stokes' type boundary value problem, which is equipped with the Beavers-Joseph (Beavers and Joseph, 1967; Jones, 1973) interface conditions (14) via the non-dimensional number

$$\phi = \frac{\sqrt{\bar{\kappa}}}{q}, \tag{17}$$

which accounts for the slip over a porous surface, where $q$ is a non dimensional parameter. According to the physiological data reported in Table 1

$$\phi \ll 1 \tag{18}$$

so that the cell problems given by (11-14) and (15-16), rewrite, componentwise:

$$\begin{cases} \dfrac{\partial^2 W_{ji}}{\partial y_k \partial y_k} + \dfrac{\partial P^c_i}{\partial y_j} + \delta_{ij} = 0 \quad \text{in } \Omega_c & (19) \\ \dfrac{\partial W_{ji}}{\partial y_j} = 0 \quad \text{in } \Omega_c & (20) \\ W_{ij} = 0 \quad \text{on } \Gamma, & (21) \end{cases}$$

$$\begin{cases} \dfrac{\partial^2 P^t_i}{\partial y_k \partial y_k} = 0 \quad \text{in } \Omega_t & (22) \\ \dfrac{\partial P^t_i}{\partial y_j} n_j = n_i \quad \text{on } \Gamma, & (23) \end{cases}$$

where $i, j, k = 1...3$ and summation over repeated indices is understood. It is worth to remark that, even though $(\mathsf{W}(\mathbf{y}), \mathbf{P}^c(\mathbf{y}))$ and $\mathbf{P}^t(\mathbf{y})$ formally satisfy classical Stokes' and Laplace type boundary value problems, they merely play the role of auxiliary variables which are to be computed to obtain the physically meaningful quantities, which are the effective conductivity tensors given by the relationships (9).

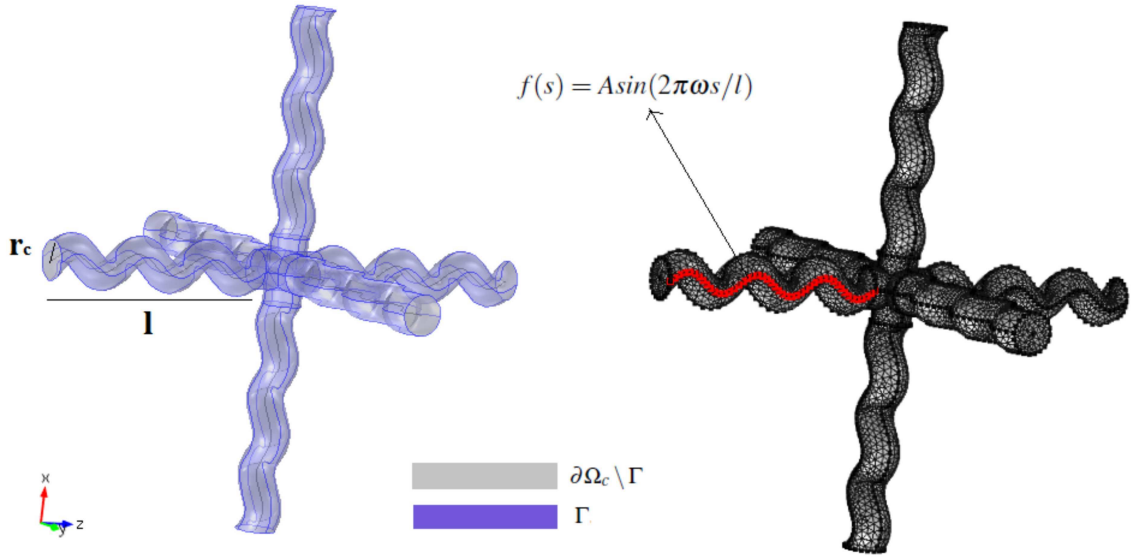


Figure 2: An example of the microscale representative capillary cell portion $\Omega_c$ and its geometric features are depicted. On the left hand side, the tortuous geometry is shown, whereas $r_c$ and $l$ correspond to the capillary radius and the one-sided branch length, respectively. The difference between the capillary (dirichlet) walls $\Gamma$ and the (periodic) outer faces $\partial\Omega_c \setminus \Gamma$ is pointed out. On the right hand side, the corresponding 3D computational mesh is shown and the analytic parametrization of the geometry is highlighted.

## 3. The microscale cell problems

### *3.1. The macroscopic isotropic setting*

The macroscopic double-Darcy problem (3-6) is isotropic when the microscale geometry satisfies the following identities:

$$\mathsf{K} = K_c \mathsf{I}, \quad K_c := \langle W_{11} \rangle_c = \langle W_{22} \rangle_c = \langle W_{33} \rangle_c \tag{24}$$

$$\mathsf{E} = E_t \mathsf{I}, \quad E_t := \langle E_{11} \rangle_t = \langle E_{22} \rangle_t = \langle E_{33} \rangle_t . \tag{25}$$

This spherical characterization of the microvascular conductivity has no physiological meaning *per se*: it enables us to account for a range of significant variations in the microstructure geometry and highlights the physical contribution of the homogenized model via a reduced number of parameters. This way, it provides quantitative results which can be compared to previous, experimentally validated isotropic models (Jain and Baxter, 1988; Boucher et al., 1990). In order to verify identities (24-25), we choose a prototypical microstructure composed of three orthogonal branches, which is invariant under permutations of the three coordinate axes (preserving right-handedness) by construction, as shown in figure 2 and 3. The differential problems for $\mathsf{W}$ (19-21) and $\mathbf{P}^t$ (22-23), are three standard Stokes' and Laplace problems for $i = 1,2,3$ respectively and we can enforce rotation invariance to compute the solution for $\mathsf{W}$ and $\mathbf{P}^t$ by solving one Stokes' and Laplace problem only. In fact we can fix, for example, $i = 3$ in (19-21) and (22-23) without loss of generality, obtaining the following cell problems:

$$\begin{cases} \nabla_{\mathbf{y}}^2 \mathbf{w} - \nabla_{\mathbf{y}} P^c + \mathbf{e}_3 = 0 \quad \text{in } \Omega_c & (26) \\ \nabla_{\mathbf{y}} \cdot \mathbf{w} = 0 \quad \text{in } \Omega_c & (27) \\ \mathbf{w} = 0 \quad \text{on } \Gamma, & (28) \end{cases}$$

$$\begin{cases} \nabla_{\mathbf{y}}^2 P^t = 0 \quad \text{in } \Omega_t & (29) \\ \nabla_{\mathbf{y}} P^t \cdot \mathbf{n} = n_3 \quad \text{on } \Gamma, & (30) \end{cases}$$

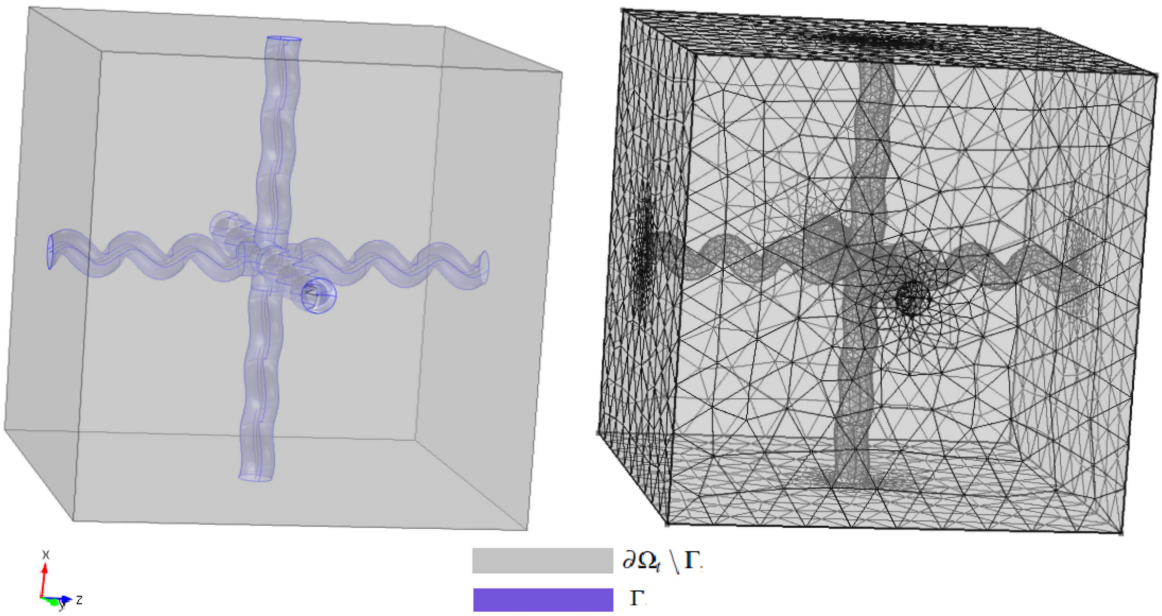


Figure 3: An example of the microscale representative interstitial cell portion $\Omega_t = \Omega \setminus \Omega_c$. On the left hand side, the tortuous geometry is shown and the difference between the (Neumann) inner walls $\Gamma$ and the (periodic) outer faces $\partial\Omega_t \setminus \Gamma$ is pointed out. On the right hand side, the corresponding 3D computational mesh is shown.

$$\langle P^c \rangle_c = 0 \quad \text{in } \Omega_c \quad \text{and} \quad \langle P^t \rangle_t = 0 \quad \text{in } \Omega_t.$$

where we explicitly set, by components:

$$w_1 = W_{13}, w_2 = W_{23}, w_3 = W_{33}, \qquad P^c = P_3^c, P^t = P_3^t. \tag{31}$$

Then, enforcing rotation invariance of the geometry with respect to the three orthogonal axes, we get

$$\begin{aligned} w_1 &= W_{13} = W_{21} = W_{32} \\ w_2 &= W_{23} = W_{31} = W_{12} \\ w_3 &= W_{33} = W_{11} = W_{22}, \end{aligned} \tag{32}$$

$$\begin{aligned} \frac{\partial P^t}{\partial y_1} &= \frac{\partial P_3^t}{\partial y_1} = \frac{\partial P_1^t}{\partial y_2} = \frac{\partial P_2^t}{\partial y_3} \\ \frac{\partial P^t}{\partial y_2} &= \frac{\partial P_3^t}{\partial y_2} = \frac{\partial P_1^t}{\partial y_3} = \frac{\partial P_2^t}{\partial y_1} \\ \frac{\partial P^t}{\partial y_3} &= \frac{\partial P_3^t}{\partial y_3} = \frac{\partial P_1^t}{\partial y_1} = \frac{\partial P_2^t}{\partial y_2} \end{aligned} \tag{33}$$

and the full solution for $\mathsf{K}$ and $\mathsf{E}$ can be recovered once definitions (9) are exploited.

In order to test the impact of the microvasculature tortuosity on the blood flow, we perform our analysis varying the geometrical configuration of $\Omega_c$ (and $\Omega_t$ accordingly). In particular, we design the center line of every branch by an analytical parametrization of the type:

$$f(s) = A \sin(2\pi\omega s/l), \tag{34}$$

| $\omega$ | $A$ | $\lvert\Omega_c\rvert$ | $\lvert\Omega_t\rvert(\lvert\Omega\rvert-\lvert\Omega_c\rvert)$ | $S$ | $K_c\,(\langle w_3\rangle_c)$ | $\langle w_1\rangle_c$ | $\langle w_2\rangle_c$ | Kozeny constant |
|---|---|---|---|---|---|---|---|---|
| 0 | 0 | $8.1\cdot10^{-2}$ | 6.149 | 2.30 | $2.20\cdot10^{-4}$ | $2.83\cdot10^{-9}$ | $2.89\cdot10^{-10}$ | 5.6 |
| 1 | $0.25r_c$ | $8.0\cdot10^{-2}$ | 6.15 | 2.30 | $2.17\cdot10^{-4}$ | $3.81\cdot10^{-8}$ | $3.53\cdot10^{-8}$ | 5.6 |
| 1 | $0.5r_c$ | $7.9\cdot10^{-2}$ | 6.151 | 2.30 | $2.06\cdot10^{-4}$ | $6.57\cdot10^{-8}$ | $6.22\cdot10^{-8}$ | 5.7 |
| 1 | $0.75r_c$ | $7.8\cdot10^{-2}$ | 6.152 | 2.31 | $1.90\cdot10^{-4}$ | $8.17\cdot10^{-8}$ | $7.86\cdot10^{-8}$ | 6.0 |
| 1 | $r_c$ | $7.6\cdot10^{-2}$ | 6.154 | 2.32 | $1.69\cdot10^{-4}$ | $8.42\cdot10^{-8}$ | $8.22\cdot10^{-8}$ | 6.3 |
| 2 | $0.25r_c$ | $7.9\cdot10^{-2}$ | 6.151 | 2.30 | $2.05\cdot10^{-4}$ | $6.26\cdot10^{-8}$ | $5.85\cdot10^{-8}$ | 5.7 |
| 2 | $0.5r_c$ | $7.6\cdot10^{-2}$ | 6.154 | 2.33 | $1.63\cdot10^{-4}$ | $8.52\cdot10^{-8}$ | $8.02\cdot10^{-8}$ | 6.5 |
| 2 | $0.75r_c$ | $7.2\cdot10^{-2}$ | 6.158 | 2.42 | $1.08\cdot10^{-4}$ | $4.64\cdot10^{-8}$ | $4.85\cdot10^{-8}$ | 8.2 |
| 2 | $r_c$ | $6.9\cdot10^{-2}$ | 6.161 | 2.57 | $6.24\cdot10^{-5}$ | $2.17\cdot10^{-8}$ | $2.30\cdot10^{-8}$ | 11.5 |
| 3 | $0.25r_c$ | $7.8\cdot10^{-2}$ | 6.152 | 2.32 | $1.84\cdot10^{-4}$ | $7.54\cdot10^{-8}$ | $7.39\cdot10^{-8}$ | 6.1 |
| 3 | $0.5r_c$ | $7.2\cdot10^{-2}$ | 6.158 | 2.53 | $7.71\cdot10^{-5}$ | $3.66\cdot10^{-8}$ | $4.51\cdot10^{-8}$ | 10.5 |
| 3 | $0.75r_c$ | $6.8\cdot10^{-2}$ | 6.162 | 2.82 | $2.02\cdot10^{-5}$ | $-2.64\cdot10^{-9}$ | $3.60\cdot10^{-9}$ | 29.0 |
| 3 | $r_c$ | $6.5\cdot10^{-2}$ | 6.165 | 3.25 | $4.89\cdot10^{-6}$ | $-2.63\cdot10^{-8}$ | $6.82\cdot10^{-9}$ | 80.0 |

Table 2: Computational results for the non-dimensional capillary hydraulic conductivity $K_c$, cell exchange surface $S$ and capillary cell volume portion $|\Omega_c|$ for thirteen cells of increasing tortuosity. Non-diagonal values of $\mathsf{K}$ are negligible with respect to $K_c$.

where $A$ represents the amplitude, $\omega$ the spatial frequency, $l$ the one-sided branch length and $s$ the local parametrization of the spatial coordinate, such that

$$0 \le s \le l,$$

as depicted in Figure 2. We identify the geometrical *tortuosity* by the two parameters $\omega$ and $A$.

Next we numerically solve the capillary and interstitial periodic cell problems (26-28) and (29-30) via the commercial library COMSOL Multiphysics. Spatial discretization is carried out by the standard Taylor–Hood ($\mathbb{P}_2/\mathbb{P}_1$) finite element pair for the Stokes' problem (26-28), whereas a $\mathbb{P}_2$ finite element discretization is used for the Laplace problem (29-30). Then, exploiting the macroscopic isotropy (24-25), the analytical solution of the macroscale model (3-6) is provided for an isolated spherical tumor.

### *3.2. The capillary cell problem*

We vary the geometrical tortuosity parameters $\omega$ and $A$ of the reference cell and numerically compute the corresponding values of $\mathsf{K}$ (in particular the diagonal component $K_c$), $S$, $|\Omega_c|$. The results are reported in Table 2.
The numerical solution of the Stokes' problem (26-28) applied to the straight cylindrical reference geometry yields a classical parabolic–type profile (Figure 4 a). In this case, the solution is non-zero in the branch directed along $\mathbf{e}_3$ only (the direction of the unit vector in the equation (26)), and it is a small perturbation of the Poiseille–type solution which is obtained analytically solving the Stokes' problem (26-28) in a single cylindrical tube, with periodic boundary conditions on the inlet and outlet, namely:

$$w_3 = \frac{r_c^2 - r_l^2}{4}, \quad w_1 = w_2 = P^c = 0, \quad 0 \le r_l \le r_c, \tag{35}$$

where $r_l$ denote the local radial coordinate. As a consequence, the maximum value $|\mathbf{w}| = w_3$ is reached in the center of the tube:

$$|\mathbf{w}|_{r_l=0} = \frac{r_c^2}{4} \approx 1.22\cdot10^{-3}, \tag{36}$$

and its average reads:

$$K_r = K_c|_{\omega=0} = \langle w_3\rangle_c\,|_{\omega=0} = \frac{1}{|\Omega_c|}\int_0^{l_c} \mathrm{d}z \int_0^{2\pi} \mathrm{d}\theta \int_0^{r_c} \frac{r_c^2 - r_l^2}{4} r_l\,\mathrm{d}r_l = \frac{\pi l_c r_c^4}{8|\Omega_c|} = 2.13\cdot10^{-4}, \tag{37}$$

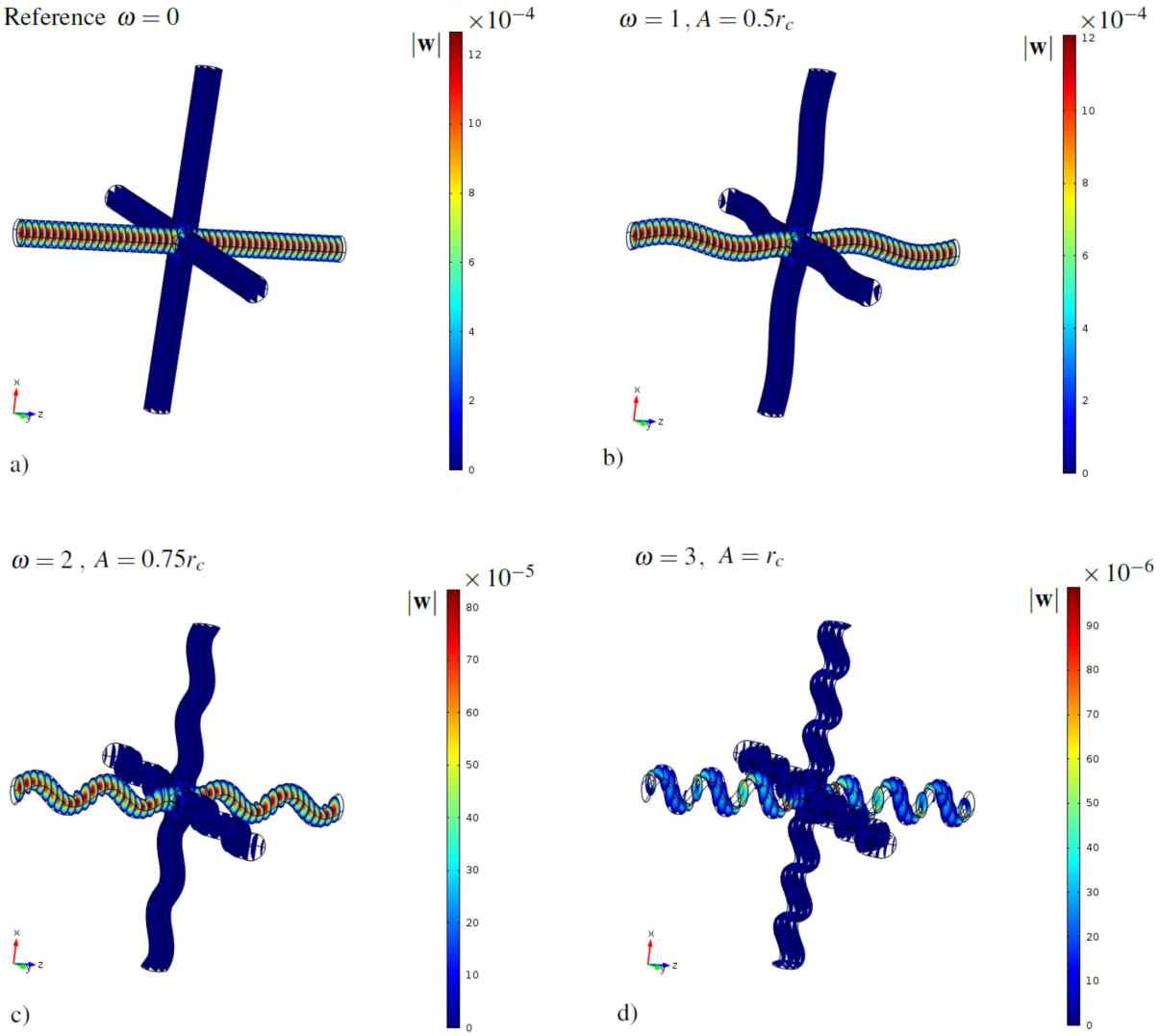


Figure 4: Color maps of $|\mathbf{w}|$ for representative geometries of increasing tortuosity. The solution retains a pseudo-parabolic profile for small pertubation in $\omega$ and $A$ of the reference configuration, whereas a sharp non-linear decrease with respect to geometrical tortuosity is observed at higher frequency.

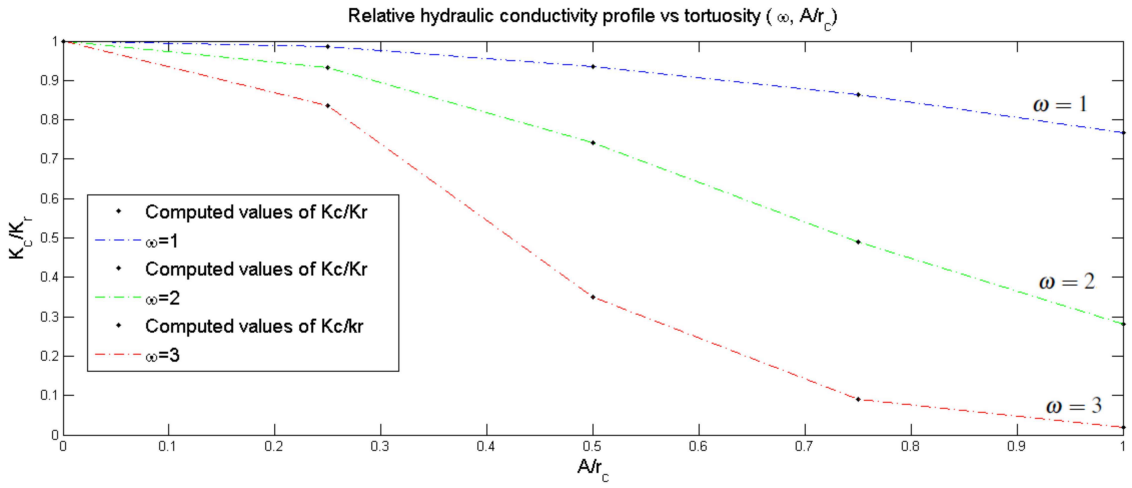


Figure 5: Relative hydraulic conductivity profile as a function of relative amplitude. The black dots represent the results of the numerical simulations, whereas dashed lines emphasize the difference in the non-linear drop of the hydraulic conductivity at increasing frequency.

where the values reported in Tables 1 and 2 have been used. In the non-tortuous case, the solution then agrees with the analytical solution (35), up to a small deviation in the central region of $\Omega_c$, where branches cross each other. [1]

The numerical solution for the computed tortuous geometric configurations deviates from a merely parabolic profile, as far as the frequency $\omega$ increases. Nevertheless, the cell average of the (non-zero) transversal components remain negligible with respect to $K_c$ (see Table 2), so that the condition (24) for macroscopic isotropy is satisfied, as

$$K_{ij} \ll K_c, \quad \forall\, i \neq j, \quad i,j = 1,2,3. \tag{38}$$

The plot of the normalized $K_c$ versus $A/r_c$ exhibits a non-linear monotonic decrease which is more marked at higher frequency $\omega$ (see Figure 5). The hydraulic conductivity $K_c$ dramatically reduces at large tortuosity and an up to 45-fold $K_c$ drop is observed.

*3.2.1. Comparison with the perturbation theory*

The observed non-linearity of the hydraulic conductivity versus tortuosity reflects the characteristics of Stokes' flow in wavy channels, where the solution can significantly deviate from the parabolic one. Nevertheless, under a number of simplifying assumptions, analytical solutions can be found by perturbative methods. Kitanidis and Dykaar (1997); Di Federico et al. (2002) developed an analytic method to determine the solution of the Stokes' problem for a 2D, axis symmmetric, periodic, waving channel, in terms of a power series expansion, under the assumption that the width is much smaller than the wavelength. They report a non-linear decrease of the flow discharge with respect to the channel amplitude at leading order whereas, to track variations with respect to the frequency, higher order terms in their asymptotic expansion should be taken into account. A 3D generalization of their theory can be found in Malevich et al. (2006), where perturbation analysis is used to calculate the waving channels permeability via power series in terms of a small asymptotic parameter, which measures the deviation of the channel with respect to a straight reference configuration. Also in that work, the authors exploit axial symmetry of the channel (which is not assumed here) and their procedure is only valid up to a critical value for their asymptotic parameter. Their result is a non-linear decrease of the channel permeability as far as its perturbation with respect to the symmetry axis increases.

The most widely exploited assumption to derive the flow field in slowly waving channels rely on the so called *lubrication* approximation (see e.g. Batchelor (2000); Malevich et al. (2006)). In such a framework, the flow is

[1] In this region, the solution in the branch directed along $z$ is not subject to homogeneous Dirichlet boundary conditions, rather, it smoothly approaches zero to match that in the orthogonal branches and, as a result, we obtain a slightly higher value for the maximum $|\mathbf{w}|_{r_l=0} \approx 1.26 \cdot 10^{-3}$ and $K_r = 2.2 \cdot 10^{-4}$. Furthermore, the components $w_1$ and $w_2$ reduce to zero up to numerical errors, namely $|w_1/w_3| \ll 1$ and $|w_2/w_3| \ll 1$ everywhere in $\Omega_c$.

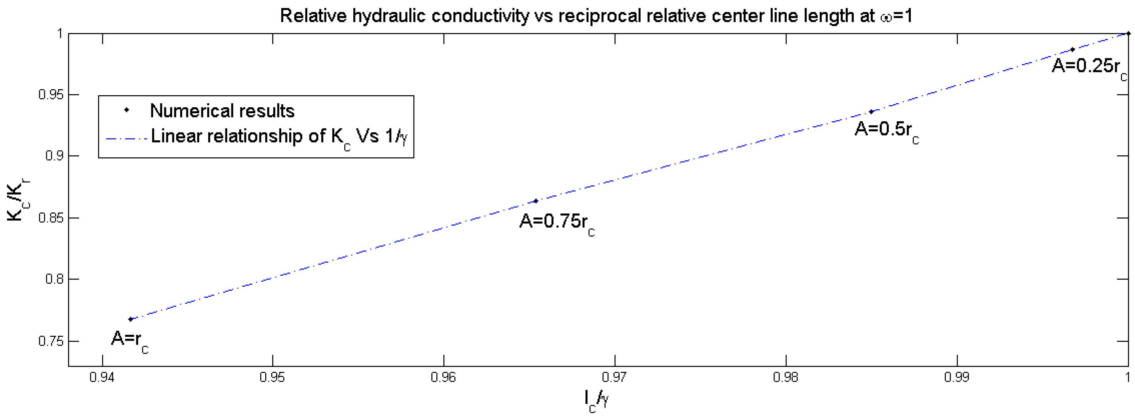


Figure 6: Numerical results showing the linear relationship between the hydraulic conductivity and the reciprocal branch center line length, in qualitative agreement with Shipley (2008).

supposed to be parabolic as long as the characteristic *length* of the channel (i.e. the wavelength for periodic geometry) is much larger than the channel height (radius) and relative variations with respect a straight reference configuration are small. For example, in Shipley (2008), curvilinear coordinates are exploited to compute the permeability of the capillary compartment; when specialized to the isotropic and non-slippery case the capillary hydraulic conductivity reads:

$$K_c = \frac{\pi r_c^4 l_c^2}{8|\Omega_c|\gamma}, \tag{39}$$

where $\gamma$ denotes the branch center line length (see Figure 2). In our case, the total branch center line length is $\gamma = 2|f| + h$, where $|f|$ denotes the one-sided branch center line length and $h$ the linking cylinder height (see Table 1). Therefore, in our reference configuration, $\gamma = l_c$ and (39) matches the analytic profile provided in (37). Notice that, for a tortuous geometrical setting, $\gamma > l_c$ and hence (39) predicts a permeability drop of the type:

$$K_c \propto \frac{1}{\gamma}. \tag{40}$$

In the high frequency regime, the lubrication approximation does not apply and the solution exhibits large deviations from the parabolic profile (see Figure 4 d). However, when $\omega = 1$, the perturbation of the geometry with respect to the reference configuration is small enough that the numerical results agree with (40) (see Figure 6).

Also the capillary network formed by the cell portions $\Omega_c$ can be viewed as a porous medium, with unit porosity and hydraulic conductivity given by the Kozeny-Carman formula (Kozeny (1927); Carman (1937); Heijs and Lowe (1995)), which in our notation reads:

$$K_c = \frac{1}{c_0 S_c^2}; \quad S_c = \frac{S}{|\Omega_c|}, \tag{41}$$

where $S_c$ is the capillary surface-to-volume ratio and $c_0$ is the so called *Kozeny constant*. According to the relationship (41), the hydraulic conductivity should therefore exhibit a quadratic decrease with respect to the surface-to-volume ratio of the porous medium. Nevertheless, $c_0$ itself can be shown to increase with the geometrical tortuosity. Matyka et al. (2008) show that the Kozeny constant exhibits a quadratic dependence on the representative path length, which is in turn related to the geometrical tortuosity. We have numerically computed the Kozeny constant for several prototype geometries (see Table 2). Whenever deviations from the reference configurations are small (i.e $\omega = 1$), a relationship of the type (41) is sufficient to describe the dependence of the capillary hydraulic conductivity on the geometrical properties of the network. Nevertheless, as the tortuosity increases, a quadratic decrease of $K_c$ with respect to the surface-to-volume ratio $S/|\Omega_c|$ is not anymore observed, as a dramatic increase of $c_0$, which is not constant any longer, is observed.

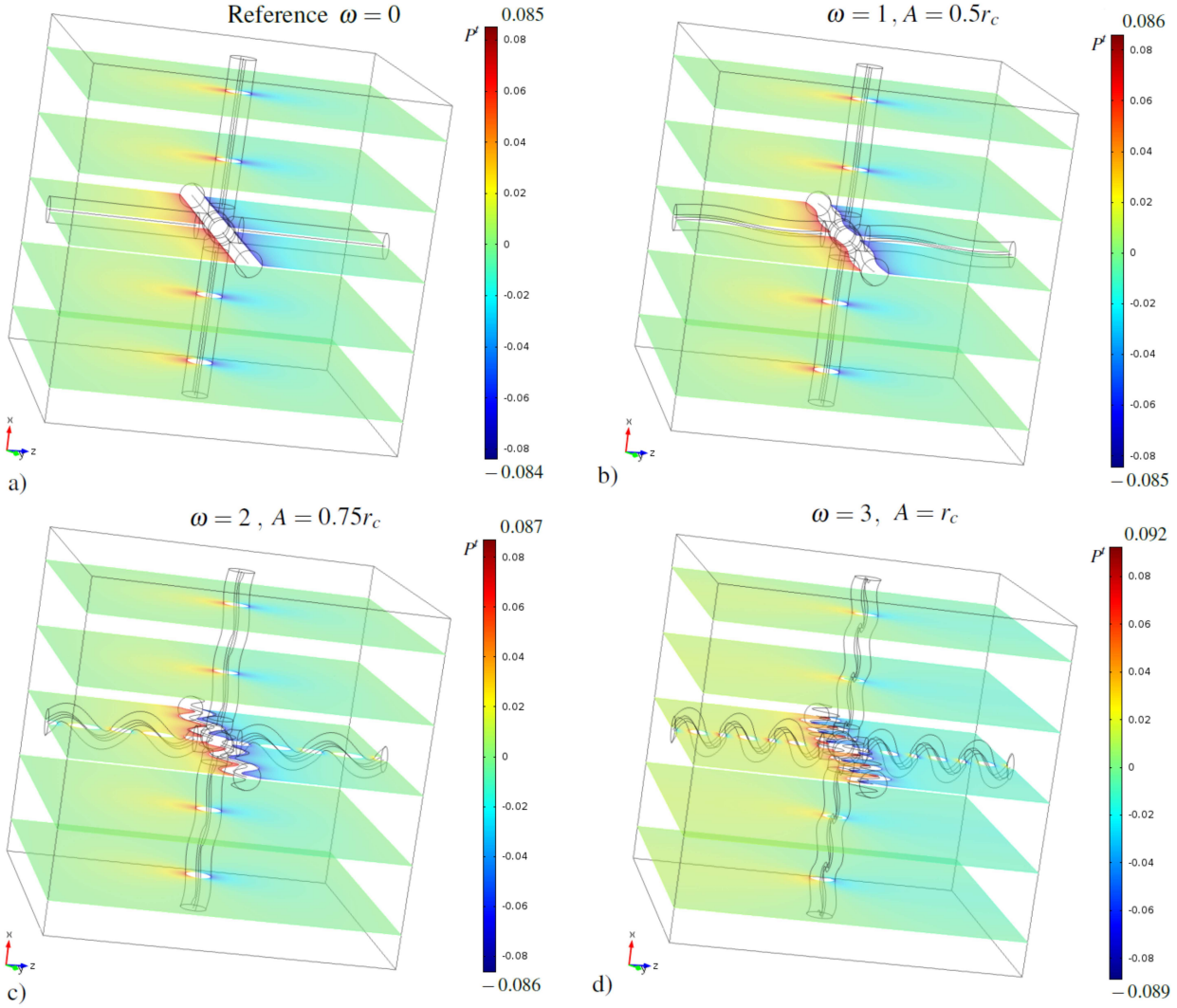


Figure 7: Color maps of $P^I$ for different representative geometries. The solution gradients only weakly contributes to the effective hydraulic conductivity $\mathsf{E}$ and no significant changes are observed by varying the geometrical tortuosity (see Table 3).

| $\omega$ | $A$ | $E_t\left(1-\left\langle\frac{\partial P^t}{\partial y_3}\right\rangle_t\right)$ | $\left\langle\frac{\partial P^t}{\partial y_1}\right\rangle_t$ | $\left\langle\frac{\partial P^t}{\partial y_2}\right\rangle_t$ |
|---|---|---|---|---|
| 0 | 0 | 0.991 | $1.23\cdot10^{-8}$ | $-6.55\cdot10^{-8}$ |
| 1 | $0.25r_c$ | 0.991 | $-2.25\cdot10^{-5}$ | $-7.35\cdot10^{-5}$ |
| 1 | $0.5r_c$ | 0.991 | $-1.40\cdot10^{-5}$ | $-1.49\cdot10^{-5}$ |
| 1 | $0.75r_c$ | 0.991 | $-1.98\cdot10^{-5}$ | $-2.02\cdot10^{-5}$ |
| 1 | $r_c$ | 0.991 | $-2.76\cdot10^{-5}$ | $-2.71\cdot10^{-5}$ |
| 2 | $0.25r_c$ | 0.991 | $-6.36\cdot10^{-6}$ | $-5.83\cdot10^{-6}$ |
| 2 | $0.5r_c$ | 0.991 | $-1.63\cdot10^{-5}$ | $-1.50\cdot10^{-5}$ |
| 2 | $0.75r_c$ | 0.992 | $-3.30\cdot10^{-5}$ | $-3.09\cdot10^{-5}$ |
| 2 | $r_c$ | 0.992 | $-5.46\cdot10^{-5}$ | $-5.23\cdot10^{-5}$ |
| 3 | $0.25r_c$ | 0.991 | $-1.00\cdot10^{-5}$ | $-6.89\cdot10^{-6}$ |
| 3 | $0.5r_c$ | 0.992 | $-5.09\cdot10^{-5}$ | $-5.24\cdot10^{-6}$ |
| 3 | $0.75r_c$ | 0.992 | $-5.48\cdot10^{-5}$ | $-3.47\cdot10^{-5}$ |
| 3 | $r_c$ | 0.992 | $1.00\cdot10^{-5}$ | $1.00\cdot10^{-5}$ |

Table 3: Computational results for the non-dimensional conductivity tensor $\mathsf{E}$. $E_t \approx 0.99$ for every tortuosity regime explored. Non diagonal values of $\mathsf{E}$ are negligible with respect to $E_t$.

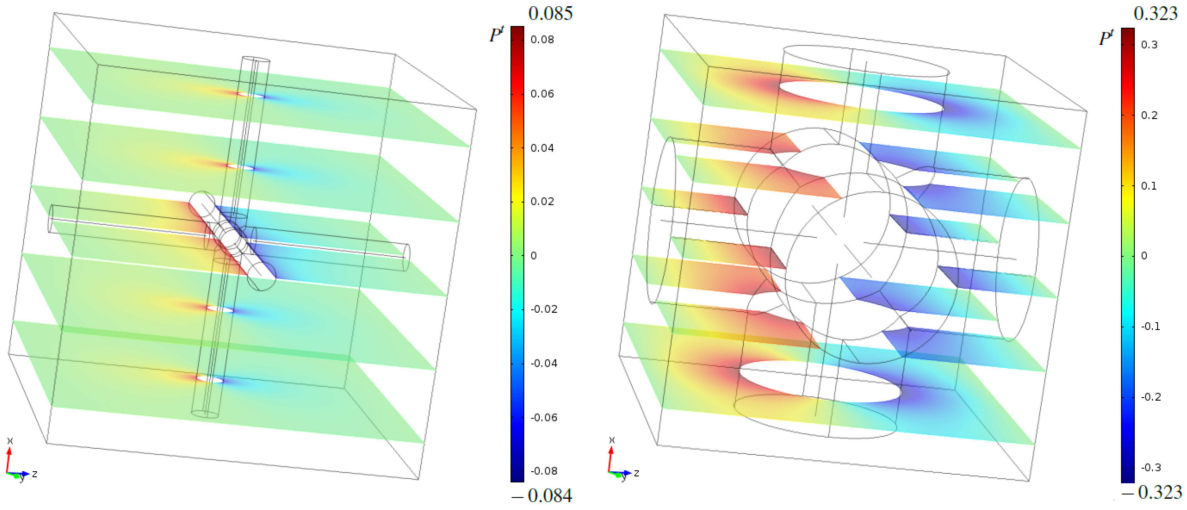


Figure 8: Color maps of $P^t$ for two non-tortuous geometries, with different $\frac{|\Omega_t|}{|\Omega|}$ ratio. On the left hand side, the reference geometry (which corresponds to the reference capillary compartment radius $r_c$) is characterized by small and localized spatial variation of the solution $\frac{\partial P^t}{\partial y_3}$. On the right hand side, the solution for $\frac{|\Omega_t|}{|\Omega|} \approx 0.64$ (which corresponds to a $6r_c$ capillary compartment radius) is shown. In the latter case, the interstitial volume fraction decreases and the spatial gradient of $P^t$ increases, thus leading to a corresponding decrease in $E_t$ (see definition (9) and Figure 9).

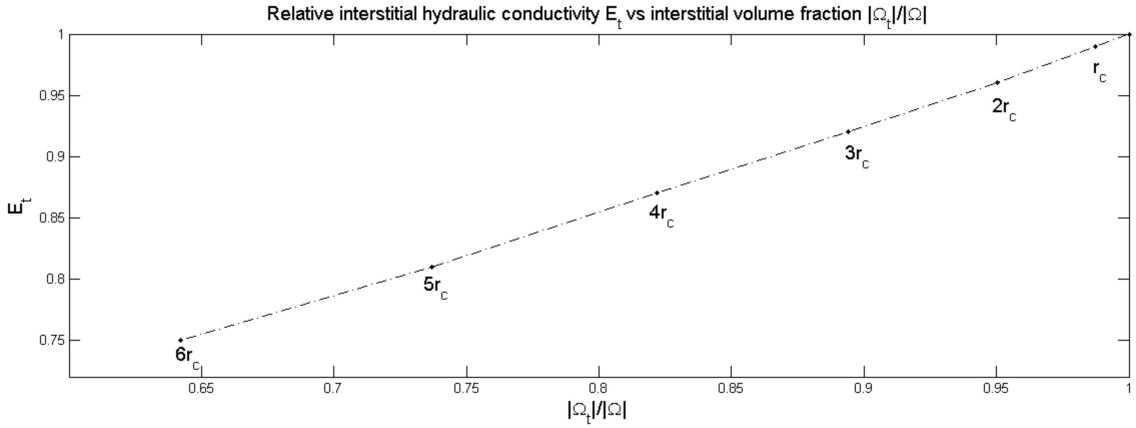


Figure 9: A linear relationship between $E_t$ and the interstitial volume fraction $\frac{|\Omega_t|}{|\Omega|}$. Black dots represent the numerical results which correspond to the various interstitial configurations obtained by varying the radius of each complementary capillary compartment branch from $r_c$ to $6r_c$.

### *3.3. The interstitial cell problem*

We perform numerical simulations to compute $P^t$ and hence capture variations of the interstitial conductivity $\mathsf{E}$ (in particular the diagonal component $E_t$) with respect to tortuosity, in the complementary geometry $\Omega_t = \Omega \setminus \Omega_c$ (see Figure 7). The numerical solution of the problem (29-30) is weakly affected by tortuosity. According to Table 3, accounting for definition (9) and identifications (33), we deduce:

$$E_{ij} \ll E_t \quad \forall\, i \neq j, \quad i,j = 1,2,3, \tag{42}$$

that is, the macroscopic isotropy condition (25) is satisfied. We further notice that, even though integral average variations of $P^t$ along $\mathbf{e}_3$ are more relevant than those in the other directions, they are however much smaller than 1, such that, in the explored regimes, $\mathsf{E}$ slightly deviates from the identity tensor. The geometric role of $E_t$ can be pointed out by decreasing the interstitial volume $|\Omega_t|$ (see Figure 8). We perform numerical tests for sample interstitial geometries $\Omega_t$. We find an almost linear relationship between $E_t$ and interstitial volume fraction (see Figure 9). We recall that according to (6) and (25) the non-dimensional interstitial velocity is given by:

$$\mathbf{u}_t = -\bar{\kappa} E_t \nabla_{\mathbf{x}} p_t, \tag{43}$$

where the non-dimensional conductivity $\bar{\kappa}$ is directly related to the physiological value $\kappa$, which is obtained via experimental measurements over the whole tumor mass (without distinction between interstitial and capillary compartment). On the basis of our numerical tests (see Figure 9), $E_t$ reads as a correction factor ($0 < E_t < 1$), which reduces the average measured conductivity value according to the actual interstitial volume portion perfused by the fluid.

In the following section, we present and discuss the analytical solution of the isotropic fluid transport problem (3-6). Since we focus on the consequences of increased geometrical tortuosity, we exploit the numerical values reported in Table 1, 2 and 3 in the analysis that follows.

## 4. The macroscopic model

The macroscale differential problem (3-6), under isotropic conditions (24-25), reads:

$$\begin{cases} \nabla^2_{\mathbf{x}} p_c = M_c(p_c - p_t) & \text{in } \Omega_H \quad (44) \\ \nabla^2_{\mathbf{x}} p_t = -M_t(p_c - p_t) & \text{in } \Omega_H \quad (45) \\ \mathbf{u}_c = -K_c \nabla_{\mathbf{x}} p_c \quad (46) \\ \mathbf{u}_t = -K_t \nabla_{\mathbf{x}} p_t, \quad (47) \end{cases}$$

where

$$K_t = E_t \bar{\kappa}, \quad M_c = \frac{\bar{L}_p S}{K_c |\Omega_c|}, \quad M_t = \frac{\bar{L}_p S}{K_t |\Omega_t|}. \tag{48}$$

We consider a spherical macroscale domain $\Omega_H$ with radius $R$ representing the tumor. We enforce radial symmetry: all the fields depend on the radial coordinate $r$ only and the problem (44-45) rewrites

$$\begin{cases} \frac{1}{r}\frac{d^2}{dr^2}(rp_c) = M_c(p_c - p_t) \qquad 0 < r < R & (49) \\ \frac{1}{r}\frac{d^2}{dr^2}(rp_t) = -M_t(p_c - p_t) \qquad 0 < r < R & (50) \\ \frac{dp_c}{dr}|_{r=0} = \frac{dp_t}{dr}|_{r=0} = 0 & (51) \\ p_c|_{r=R} = \bar{p} > 0, \quad p_t|_{r=R} = 0. & (52) \end{cases}$$

The tumor is supposed to be isolated (Jain and Baxter, 1988; Jain et al., 2007): a malignant (possibly vascularized) mass such that the interaction with th environment occurs only through possible drugs transported by the microvasculature. This system is therefore isolated with respect to surrounding organs, both from a biomolecular (degradation) and from a mechanical (stress) point of view. Hence, we prescribe the pressures on the tumor boundary (52), while symmetry in $r = 0$ implies null flux in the tumor center, corresponding to homogeneous Neumann boundary conditions (51). The choice (52) accounts for experimental observations (Boucher et al., 1990): the interstial fluid pressure is constant and smaller than the microvasculature pressure on the tumor surface. The flow driving force is the pressure difference $p_c - p_t$ and $p_t$ can be set to zero on the tumor surface without loss of generality (Jain and Baxter, 1988; Jain et al., 2007). The radial components of the Darcy's velocities $u_c(r)$ and $u_t(r)$ are

$$u_c(r) = -K_c \frac{dp_c}{dr}, \quad u_t(r) = -K_t \frac{dp_t}{dr}. \tag{53}$$

The solution of the problem (49-52) can be obtained via direct integration (see Appendix A):

$$\hat{p}_c = \frac{1}{M_c + M_t}\left(M_t + \frac{M_c \sinh(\alpha\hat{r})}{\hat{r}\sinh(\alpha)}\right), \tag{54}$$

$$\hat{p}_t = \frac{M_t}{M_c + M_t}\left(1 - \frac{\sinh(\alpha\hat{r})}{\hat{r}\sinh(\alpha)}\right), \tag{55}$$

where $\hat{p}_c = p_c/\bar{p}$, $\hat{p}_t = p_t/\bar{p}$ are the relative capillary and interstitial pressure, respectively and $\hat{r} = r/R$ is the relative radial position, while

$$\alpha = R\sqrt{(M_c + M_t)}. \tag{56}$$

The capillary and interstitial velocities can be written in terms of

$$\hat{u}_c = \frac{u_c R}{K_r \bar{p}}, \quad \hat{u}_t = \frac{u_t R}{K_t \bar{p}} \tag{57}$$

by direct derivation:

$$\hat{u}_c = -\frac{K_c M_c}{K_r(M_c + M_t)}\left(\frac{\alpha\hat{r}\cosh(\alpha\hat{r}) - \sinh(\alpha\hat{r})}{\sinh(\alpha)\hat{r}^2}\right), \tag{58}$$

$$\hat{u}_t = \frac{M_t}{M_c + M_t}\left(\frac{\alpha\hat{r}\cosh(\alpha\hat{r}) - \sinh(\alpha\hat{r})}{\sinh(\alpha)\hat{r}^2}\right). \tag{59}$$

Finally, we define the relative pressure difference between the capillary and interstitial pressure as

$$\hat{\psi} = \hat{p}_c - \hat{p}_t = \frac{\sinh(\alpha\hat{r})}{\hat{r}\sinh(\alpha)}. \tag{60}$$

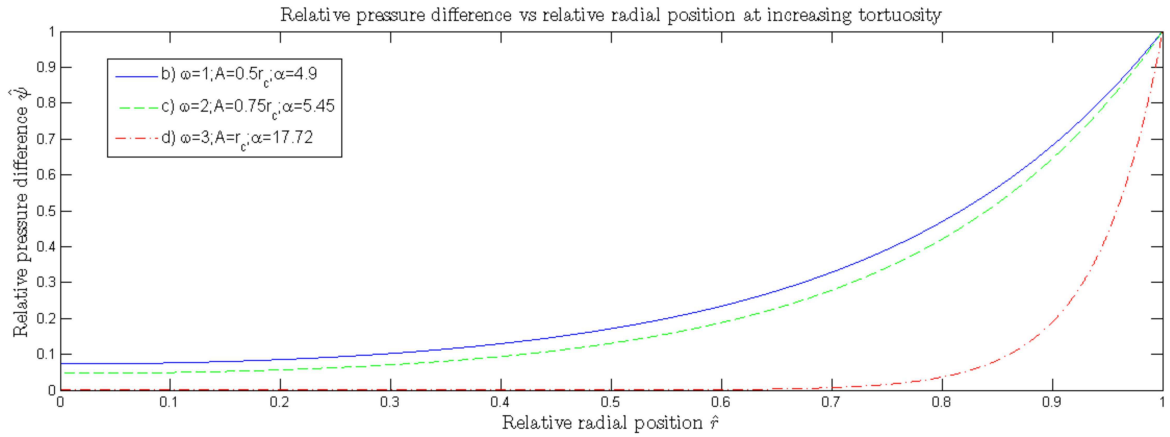


Figure 10: The macroscopic pressure difference is plotted versus the relative radial position. The results are plotted for the tortuous microvasculatures b, c and d (see Figure 4). The solution exhibits a sharp non-linear decreasing profile at increased tortuosity (the latter implying an increase in $\alpha$), such that, for high geometrical complexity, no pressure difference and hence no convection of blood is observable in the tumor inner regions.

### *4.1. The impact of tortuosity on tumor blood convection*

The relative pressure difference is plotted versus the relative radial position (see Figure 10). The relative pressure jump $\hat{\psi}$ is the driving force of the blood flow (see Figure 11 and 12) and exponentially decays versus $1/\alpha$, where

$$\alpha = R\sqrt{\frac{\bar{L}_p S}{|\Omega_c|K_c} + \frac{\bar{L}_p S}{|\Omega_t|K_t}}. \tag{61}$$

As far as the tortuosity of the microvasculature grows, the surface to capillary volume ratio $S/|\Omega_c|$ increases, while the hydraulic conductivity $K_c$ decreases (see Table 2), both contributing to an increase in $\alpha$. In fact, for low tortuosity (i.e in the $\alpha < 5$ regime, see Figure 10), a non-zero pressure difference is observed even in the tumor center whereas, for higher values of $\alpha$ blood and possible injected anti-cancer drugs cannot permeate the whole tumor mass. For example, in the most tortuous regime that we explore, no blood flow can permeate the tumor mass for $\hat{r} \simeq 0.7$.

The main feature of our multiscale formulation is to account for the hydraulic and geometric properties of the tissue interstitium and capillary compartment separately, such that, under fixed physiological conditions (see Table 1), we can quantitatively evaluate the role of the geometrical tortuosity in tumor blood convection. Even though we perform the present analysis accounting for a specific microscale configuration, we argue that our results are robust with respect to different geometric settings, provided that conditions (24-25) are met. Given the physiological set of parameters encoded in the number $\alpha$ (the tumor radius $R$, vascular hydraulic permeability $L_p$ and tumor tissue conductivity $\kappa$), we thus predict a strong dependence of the tumor blood convection with respect to tortuosity, such that geometrical regularization of the microvasculature network can improve blood flow within the tumor. Next, we compare the results of our model with the relevant literature and perform an analysis of the blood flow determinants which are captured by these different formulations.

## 5. Comparison with Jain and Baxter (1988)

The model for fluid flow in a spherical solid tumor developed by Jain and Baxter (1988) and experimentally validated by Boucher et al. (1990) is based on a single compartment for the interstitial flow, which exchange fluid through the blood vessels walls. i In particular, the interstitial velocity $\mathbf{u}_I$ is given by the isotropic Darcy law:

$$\mathbf{u}_I = -\kappa \nabla p_I, \tag{62}$$

where $p_I$ is the interstitial pressure. The fluid leakage from the blood vessels is an effective source for the interstitial flow:

$$\nabla \cdot \mathbf{u}_I = \frac{J_V}{\mathrm{V}}, \tag{63}$$

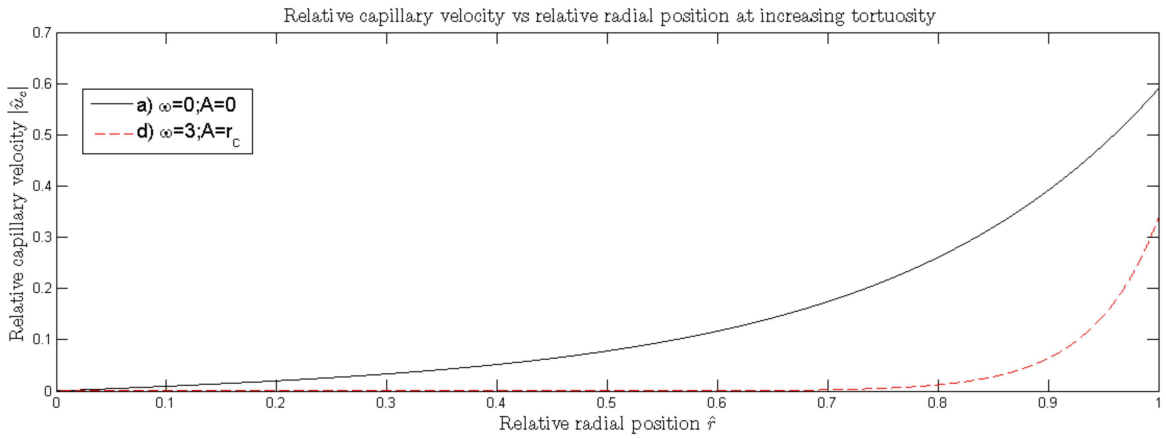


Figure 11: The relative capillary velocity is plotted versus the relative radial coordinate for the reference (Figure 4 a) and most tortuous configuration (Figure 4 d).The blood flow, driven by the pressure difference $\hat{\psi}$, is impaired by tortuosity and rapidly approaches zero.

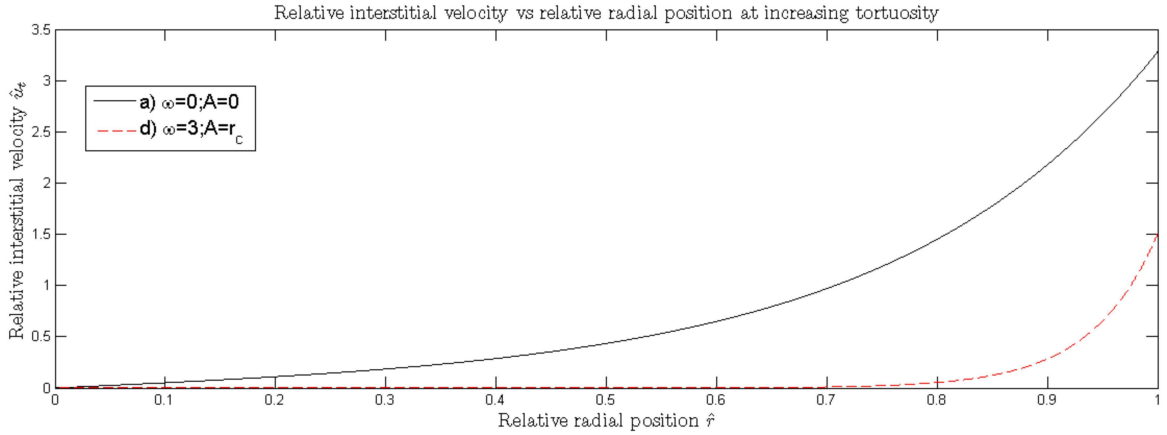


Figure 12: The relative interstitial velocity is plotted versus the relative radial coordinate for the reference (Figure 4 a) and most tortuous configuration (Figure 4 d).The blood flow, driven by the pressure difference $\hat{\psi}$, is impaired by tortuosity and rapidly approaches zero.

where V is the tumor volume and $J_V$ is the vessels blood flux:

$$J_V = L_p \mathrm{S}\,(p_V - p_I)\,, \tag{64}$$

$p_V$ being the constant microvascular pressure and S the exchange surface. The relationship (64) rules out the contribution due to the osmotic pressure driven by the plasma proteins difference in concentration, which is negligible in tumors (Jain et al., 2007). Thus, substituting (62) and (64) into (63), they obtain, in dimensional form:

$$\nabla^2 p_I = -\frac{L_p \mathrm{S}}{\kappa \mathrm{V}}\,(p_V - p_I)\,. \tag{65}$$

When assuming spherical symmetry with null interstitial pressure on the tumor boundary, the analytical solution of the model (65) for the relative interstitial pressure $p_I/p_V$ in terms of the radial coordinate $\hat{r}$ is:

$$\frac{p_I}{p_V} = 1 - \frac{\sinh(\alpha_J \hat{r})}{\hat{r}\sinh(\alpha_J)}, \tag{66}$$

where

$$\alpha_J = \mathrm{R}\sqrt{\frac{L_p \mathrm{S}}{\kappa \mathrm{V}}}. \tag{67}$$

Jain and Baxter (1988) do not address the fluid dynamics in the vessels. Nevertheless, a comparison with the model proposed in this paper in terms of relative pressure difference is possible, in fact:

$$\frac{p_V - p_I}{p_V} = \frac{\sinh(\alpha_J \hat{r})}{\hat{r}\sinh(\alpha_J)}. \tag{68}$$

The pressure drop in (60) and (68) have the same functional form; however, the non dimensional coefficients $\alpha$ and $\alpha_J$ are different, as in this work we explicitly account for variations in the capillary pressure and for the role of the specific geometric and hydraulic vessels properties, such as their volume and hydraulic conductivity. In particular, the model by Jain and Baxter (1988) can be recovered when assuming that the capillary pressure is constant and

$$|\Omega_c| K_c \gg |\Omega_t| K_t, \quad |\Omega_t| \approx |\Omega| \rightarrow E_t \approx 1, \tag{69}$$

i.e. when accounting for a geometrically regular, low density, vascular network. For example, according to Tables 1, 2 and 3, we obtain $|\Omega_c| K_c \approx 5|\Omega_t| K_t$ and $|\Omega_t| \approx |\Omega|$ with $E_t \approx 1$ for our reference configuration. Whenever the conditions (69) apply, we obtain

$$\alpha \approx R\sqrt{\frac{\bar{L}_p S}{\bar{\kappa}|\Omega|}} = R\sqrt{\frac{L_p S L^2}{\kappa d |\Omega|}}, \tag{70}$$

where definitions (7) are exploited. The dimensional exchange surface to volume ratio and tumor radius read:

$$\frac{\mathrm{S}}{\mathrm{V}} = \frac{S}{d|\Omega|}, \quad \mathrm{R} = RL, \tag{71}$$

respectively, where $R$ is the non-dimensional macroscale tumor radius, while the non-dimensional surface-to-volume ratio $S/|\Omega|$ is calculated over the microscale periodic cell. Thus, substituting (71) into (70) yields

$$\alpha \approx \mathrm{R}\sqrt{\frac{L_p \mathrm{S}}{\kappa \mathrm{V}}} = \alpha_J, \tag{72}$$

in agreement with relationship (67). The mathematical model by Jain and Baxter (1988) thus coincides with the homogenized model by Shipley and Chapman (2010) under the specific assumptions (69).

The main difference between the two models is represented by the additional information we are able to capture about the geometric and hydraulic properties of the microvascular network, as well as the spatial dependence of the capillary flow in the vessels. As the same functional form for the problem solution is obtained (see equations (60) and (68)) in both approaches, then an experimental datum fit by a relationship of the type (68) necessarily involves a dependence on the vascular microstructure, although not explicitly encoded in their non-dimensional number $\alpha_J$.

We conclude the section discussing the role of the tumor blood convection determinants captured by the two models.

- The *Tumor growth stage*, identified by the tumor radius $R$, can significantly affect fluid convection in tumors. Normalization therapies able to reduce the tumor radius can therefore strongly improve transport of blood, and, as a consequence, anti-cancer drugs within the tumor mass, thus possibly increasing medical therapies effectiveness. The tumor radius has exactly the same impact on the tumor fluid dynamics in both models.

- The *Tumor hydraulic conductivity* $\kappa$ regulates the amount of fluid that can actually permeate the tissue, hence, as expected, an increase in the tumor conductivity yields a decrease in $\alpha$, which in turn drives a convection improvement. It plays a similar quantitative role in both models, as we did not observe a significant dependence on tortuosity (see Table 3). Nevertheless, we remark that the hydraulic conductivity values are obtained by experimental measurements (see e.g. Boucher et al. (1998)) and they intrinsically refer to the whole tumor tissue. Our $K_t$ (see definitions (48)) corresponds, instead, to the interstitial conductivity only and it is in general a fraction of the average tumor conductivity value that can be experimentally measured. According to Jain et al. (2007), it is an open issue whether normalization therapies can play a role in increasing the tumor hydraulic conductivity; recently developed techniques do not highlight a significant increase of the tumor hydraulic conductivity, which is instead proved to strongly depend on the interstitial matrix constituents and hydration (Swabb et al., 1974; Jain, 1987).

- The *vascular hydraulic permeability* $L_p$ is the key determinant of the blood leakage from the capillary vessels to the tissue. It provides an averaged information on the fenestrations of the membrane, which, especially in tumors, exhibits openings and defects among the endothelial cells (Hashizume, 2000). Our model leads to the same, at a first sight counterintuitive, conclusion by Jain et al. (2007): an increase in vascular permeability does not the improve blood convection within the tumor, because leakage rapidly damps the pressure gradient across the vessels walls, which is the driving force of the blood convection process. The vascular hydraulic permeability is found to be up to two orders of magnitude greater in tumors than in healthy vascularized tissue and, according to Jain et al. (2007), vascular normalization therapies should significantly lower it.

- *The exchange surface-to-volume ratios*, here denoted by $S/|\Omega_t|$ and $S/|\Omega_c|$, play an important role in driving the fluid transport process. In the double compartment model we started from, we are able to track both the interstitial and the capillary surface-to-volume ratios. As expected, for fixed interstitial and capillary volume, a greater vascular surface leads to an increase in leakage, thus producing the same net effect of an increase in the vascular hydraulic permeability $L_p$. In Jain and Baxter (1988), the global surface-to-volume ratio plays a similar role, even though it refers to the volume of the whole tumor, instead of the interstitial portion only. According to Jain et al. (2007), vascular normalization therapies should decrease the global surface-to-volume ratio.

- *The capillary hydraulic conductivity*, here denoted by $K_c$, accounts for the hydraulic properties of the capillary network. It is a main feature captured by the homogenized model by Shipley and Chapman (2010) and neglected in the previous literature. The capillary hydraulic conductivity is strongly affected by the geometrical complexity of the network (see Figure 5). A decrease in $K_c$ corresponds to an increase in $\alpha$ (see Table 4), resulting in a compromised blood flow within the tissue. Thus, geometric regularization of the vascular network can improve both directly (through the exchange surface-to-volume ratios) and indirectly (through $K_c$, see Table 2) the fluid transport process in the malignant mass.

## 6. Tracer transport

We now aim to show that impaired tumor blood flow can significantly affect the drug delivery process. We exploit the more general drug transport model derived by Shipley (2008); Shipley and Chapman (2010), which is based on a non-dimensional double advection-diffusion-reaction model for the zeroth order interstitial and capillary concentrations $c_t$ and $c_c$. We focus on the general consequences of (possibly impaired) blood convection on the amount of drug that can penetrate the tumor mass. Therefore, an agent-specific drug transport analysis is beyond the

| $\omega$ | $A$ | $\alpha$ |
|---|---|---|
| 0 | 0 | 4.86 |
| 1 | $0.25r_c$ | 4.87 |
| 1 | $0.5r_c$ | 4.9 |
| 1 | $0.75r_c$ | 4.96 |
| 1 | $r_c$ | 5.02 |
| 2 | $0.25r_c$ | 4.90 |
| 2 | $0.5r_c$ | 5.05 |
| 2 | $0.75r_c$ | 5.45 |
| 2 | $r_c$ | 6.25 |
| 3 | $0.25r_c$ | 4.97 |
| 3 | $0.5r_c$ | 5.89 |
| 3 | $0.75r_c$ | 9.05 |
| 3 | $r_c$ | 17.72 |

Table 4: Computed values of $\alpha$ for thirteen sample microvasculature geometries. At increasing tortuosity, a typical tumor pressure difference profile is obtained, even accounting for a normalized value of the vascular hydraulic permability $L_p$.

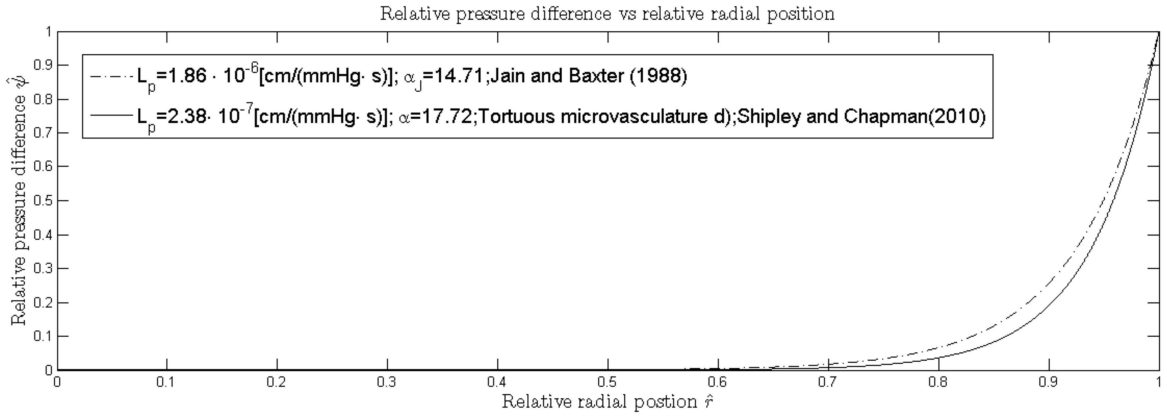


Figure 13: A comparison between the models by Jain and Baxter (1988), displayed for a tipical tumor value of $L_p$ and Shipley and Chapman (2010), displayed for a typical normalized value of $L_p$, at high tortuosity (Figure 4 d). According to Jain et al. (2007), the characteristic tumor pressure difference, which is fit approximately in the range $7 < \alpha_J < 17$ (see Table 1 for the definition of $\alpha_J$, which does not include any information about the capillaries hydraulic properties), can be the result of both increased vascular hydraulic permeability $L_p$ and of increased microvascular tortuosity.

scope of this work, so that we account for tracer molecules transport only, that is, uptake rates (which strongly depend on the specific anti-cancer agent) are ignored. Hence, for every $\mathbf{x} \in \Omega_H$ and for every $t \in (0,T)$, we have

$$\begin{cases} \dfrac{\partial c_c}{\partial t} + \nabla_{\mathbf{x}} \cdot (c_c \mathbf{u}_c) = -\dfrac{S\bar{\Upsilon}}{|\Omega_n|}(c_c - c_t) & (73) \\ \dfrac{\partial c_t}{\partial t} + \nabla_{\mathbf{x}} \cdot (c_t \mathbf{u}_t) = \dfrac{S\bar{\Upsilon}}{|\Omega_t|}(c_c - c_t), & (74) \end{cases}$$

where $(0,T)$ is a suitable time interval, whereas $\mathbf{u}_c$ and $\mathbf{u}_t$ are the capillary and interstitial velocities given by (5) and (6), respectively. Here

$$\bar{\Upsilon} = \frac{PL}{Ud}, \tag{75}$$

where $P$ is the vessel walls diffusive permeability and $U$ the characteristic capillary velocity. The system of differential equations (73-74) describes the homogenized advection of drugs and the effective role of the solute transfer between the interstitial and capillary compartment, which is proportional to the concentration drop. According to Shipley and Chapman (2010), diffusion is an higher order term. Nevertheless, even though the drug transport problem is in general dominated by advection on the tissue scale, diffusion does play a physiological role (Jain and Baxter, 1988) and, as also suggested in Shipley (2008), it is convenient to include a constant diffusivity to stabilize the system of equations (73-74), provided that advection dominates over diffusion on the macroscale, i.e. the macroscale diffusion coefficient $D_g$ satisfies:

$$Pe_g = \frac{UL}{D_g} \gg 1, \tag{76}$$

where $Pe_g$ is the global Péclet number.

Enforcing spherical symmetry, the problem (73-74), when setting diffusion according to (76), reads, for every $t \in (0,T)$:

$$\begin{cases} \dfrac{\partial c_c}{\partial t} + \dfrac{1}{r^2}\dfrac{\partial}{\partial r}\left(r^2\left(c_c u_c - \dfrac{1}{Pe_g}\dfrac{\partial c_c}{\partial r}\right)\right) = -\dfrac{S\bar{\Upsilon}}{|\Omega_n|}(c_c - c_t) \qquad 0 < r < R & (77) \\ \dfrac{\partial c_t}{\partial t} + \dfrac{1}{r^2}\dfrac{\partial}{\partial r}\left(r^2\left(c_t u_t - \dfrac{1}{Pe_g}\dfrac{\partial c_t}{\partial r}\right)\right) = \dfrac{S\bar{\Upsilon}}{|\Omega_t|}(c_c - c_t) \qquad 0 < r < R & (78) \\ \left(c_c u_c - \dfrac{1}{Pe_g}\dfrac{\partial c_c}{\partial r}\right)|_{r=0} = \left(c_t u_t - \dfrac{1}{Pe_g}\dfrac{\partial c_t}{\partial r}\right)|_{r=0} = 0 & (79) \\ c_c|_{r=R} = c_t|_{r=R} = \exp(-t/\tau) & (80) \\ c_c|_{t=0} = c_t|_{t=0} = 0, & (81) \end{cases}$$

where the radial components of the interstitial and capillary velocities $u_t$ and $u_c$ are given by the solution of the fluid transport problem and follow from the relationships (57-59). We assume that the interstitial concentration is driven by a drug capillary concentration of the type (80), which represents a *bolus* injection in the vessels, i.e. the capillary concentration decreases exponentially according to a plasma clearance time costant (Jain and Baxter, 1988). Symmetry in $r = 0$ implies null drug flux in the tumor center, corresponding to the homogeneous Neumann boundary conditions (79).

We perform numerical simulations of the system (77-81) by means of the commercial library COMSOL Multiphysics, using a $\mathbb{P}_2$ finite element discretization in space, together with the *BDF* (Backward differentiation formula) time integration method, initialized according to conditions (81). The solutions for $c_c$ and $c_t$ are computed for two limit cases, to emphasize the role of the microvascular tortuosity in the drug delivery process, namely the reference configuration (Figure 4, microvasculature a) and the most tortuous configuration (Figure 4, microvasculature d). We therefore exploit the computational data reported in tables 2 and 3 for the reference ($\omega = 0, A = 0$) and tortuous ($\omega = 3, A = r_c$) configurations, whereas we refer to Table 1 for quantities that are not affected by tortuosity.

The numerical results cleary show that both the capillary and the interstitial drug dynamics are strongly affected by the microvascular tortuosity within the chosen time interval, which corresponds to 96 hours (see Figures 14 and 15). Setting the plasma clearance time equal to 6 hours, after 24 hours the drug concentration on the boundary approaches

zero, whereas it is still possible to track the advection of drug that enters the tumor mass, from the boundary to the tumor center. For a geometrically regular microvasculature, a significant fraction of the injected drug concentration can actually reach the tumor center before being washed out from the tissue (in the presented example $\approx 40\%$ after 48 hours and $\approx 25\%$ after 96 hours). For a highly tortuous microvasculature, fluid convection is dramatically impaired and most of the injected drug is washed out before reaching the tumor inner regions (in the presented example, after 48 hours the concentration in the center is $\approx 10\%$ of the injected one).

As our work is mainly focused on the fluid transport analysis, we presented this example to simply show that compromised blood convection can dramatically decrease the amount of drug that can actually penetrate the tumor mass. However, it is worth remarking that physiological parameters can greatly vary, depending on the specific injected molecule. Therefore, a thorough analysis of the drug transport problem itself should explore a wide range of the relevant parameters, as well as account for drug comsumption and more realistic drug transfer conditions across the vessels, which are here merely related to the concentration drop (see, e.g. Jain and Baxter (1988) and Penta et al. (2014a), where both the diffusive component, which is proportional to the concentration difference and the convective component, which is related to the fluid flux filtered from the blood vessels to the tissue, are taken into account, from a biophysical and mathematical modelling viewpoint, respectively).

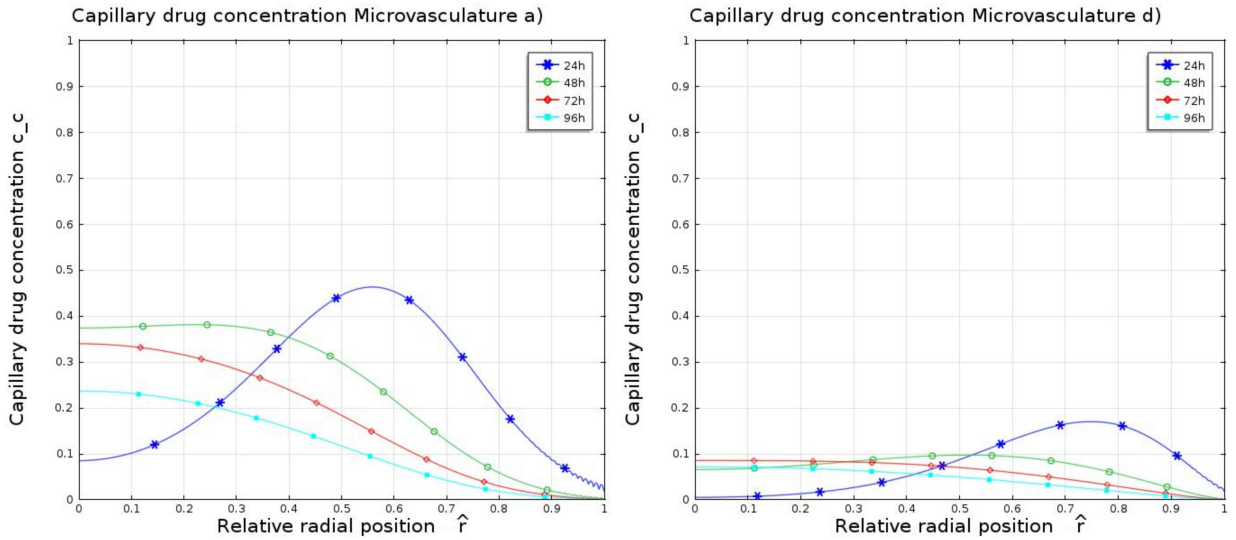


Figure 14: Capillary drug concentration profile for a regular microvasculature (left) (see Figure 4 a) and a highly tortuous one (see Figure 4 d) (right). Both solutions are plotted as functions of the relative radial position at 24, 48, 72 and 96 hours.

## 7. Concluding remarks

In this work we have performed a qualitative and quantitative analysis of the impact of microvascular tortuosity on blood convection in solid isolated tumors. We start from the double Darcy homogenized model by Shipley and Chapman (2010), to describe the tissue scale fluid dynamics of both the interstitial and capillary compartments. Although this model neglects important features of the blood flow in the capillaries, such as non-Newtonian effects (see e.g. Fahareus and Lindqvist (1931), Pries et al. (1990)), structural adaptation, remodeling of the network (see for example Pries et al. (1998); Owen et al. (2008)) and macroscopic changes of the microstructure (Penta et al., 2014a), it represents a robust starting point to account for the net effect of the tortuosity on blood transport phenomena, as it allows to track the interstitial and capillary compartment separately, as well as their hydraulic properties and their dependence on the microstructure. In this work, the geometric information encoded in the hydraulic conductivities of the model is obtained via 3D numerical simulations on a single representative microscale cell. Then, the computed values are injected in the tissue scale homogenized model, which we solve analytically in the case of macroscopic

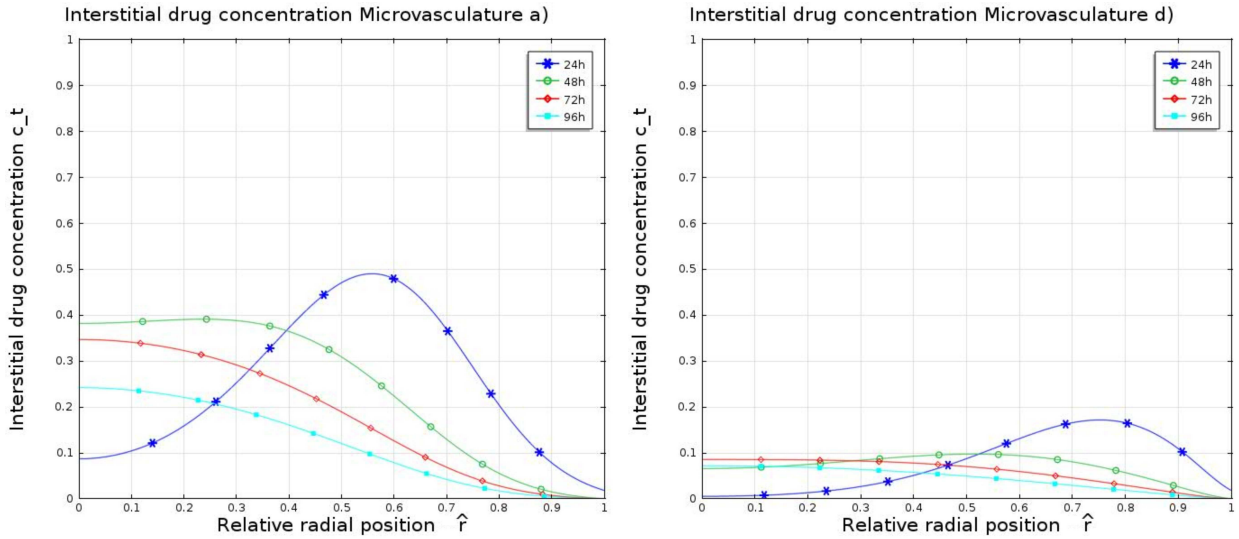


Figure 15: Interstitial drug concentration profile for a regular microvasculature (see Figure 4 a) (left) and a highly tortuous one (see Figure 4 d) (right). Both solutions are plotted as functions of the relative radial position at 24, 48, 72 and 96 hours.

isotropy. As a result, we predict a dramatically impaired blood convection for increasing tortuosity, which can be properly quantified as a function of the specific microvasculature geometry (see Table 4).

According to Jain et al. (2007), vascular normalization therapies regularize the exchange surface of the vascular network. However, our analysis suggests that modifications in the microvascular geometry strongly affect the blood flow in the capillaries and hence the hydraulic properties of the vessels compartment. In Figure 13 we show a comparison between the Jain and Baxter (1988) and Shipley and Chapman (2010) relative pressure difference profile, obtained using different values for the vascular hydraulic permeability. Curves are plotted using a $L_p$ value associated to tumor vessels (Jain et al., 2007) for Jain and Baxter (1988), whereas we use a lower $L_p$ value (corresponding to the range for normalized microvasculature, see Table 1) for Shipley and Chapman (2010), using the more tortuous configuration displayed in Figure 4d. Observing that $L_p$ is experimentally evaluated as the ratio between the average blood flux and pressure difference (both assumed constant, see e.g. Sevick and Jain (1991)), we argue that its decrease observed after normalization therapies by means of the single compartment model of Jain and Baxter (1988) actually encloses an increase in the capillary hydraulic conductivity. In other words, the same profile for the convection of blood in the tumor is obtained either accounting for a higher value of $L_p$, neglecting an explicit contribution of the microvascular properties, or accounting for a normalized $L_p$, accounting for a highly tortuous microvasculature.

Our analysis suggests that recent normalization techniques (Jain et al., 2007) affect both these crucial blood flow determinants. The observed decrease of the surface-to-volume ratio does affect the fluid-dynamics in the blood capillaries, whereas a reduction of the vessel wall openings and defects lowers $L_p$. We suggest that novel normalization therapies that rely on blood convection improvement via vascular network regularization, should focus both on structural (i.e. $L_p$) and geometrical (i.e. $K_c$, $S/|\Omega_c|$, $S/|\Omega_t|$) vessel properties.

The present model is certainly open to improvement. The assumption of a periodic vascular network, which is necessary to actually compute the microstructural problems that arise from the multiple scales homogenization, should be relaxed in future work. Although there has been some effort to address this issue, some (local) regularity of the microstructure is intrinsically required, in general, to develop a multiscale homogenized model whose coefficients explicitly comprise geometrical information. In particular, the microstructure cannot be randomly distributed in space, although the representative cell could vary with respect to every point of the homogenized domain (Holmes, 1995; Penta et al., 2014a,b). However, alternative techniques which are more flexible in this respect, such as volume averaging (see, e.g. Davit et al. (2013)), do not typically encode geometrical information in the homogenized coeffcients, which are therefore to be experimentally fitted.

From a biophysical viewpoint, the current version of the model should be also improved by explicitly taking

into account the mechanical behavior of the tumor mass and its interplay with the surrounding (healthy) organs and vasculature.

A very important development of the theory resides in a detailed analysis of the drug transport problem with respect to various anti-cancer agents (as also remarked in section 6), as well as nanomolecule (Taffetani et al., 2014), which would also help to clarify the range of clinical applicability of vessels normalization therapies.

Finally, although the aim of this work is to elucidate the connection between blood convection and vascular struscture, a next crucial and challenging step is to identify a realistic representative microscale network starting from medical images. Then, model predictions would enable clinical validation and highlight additional structure-specific blood flow features, related to possible microvascular anisotropy and heterogeneities.

**Acknowledgments**

This paper has been supported by the ERC Advanced Grant *Mathcard* (number 227058), P.I. Professor Alfio Quarteroni. We acknowledge Alessandro Lucantonio, Pietro Mascheroni and Rebecca J. Shipley for very useful hints and discussions about the content of this work.

## Appendix A. Analytical solution of the macroscale model

The problem to be solved is the following coupled system of second order differential equations of the form:

$$\begin{cases} \dfrac{1}{r}\dfrac{d^2}{dr^2}(rp_c) = M_c(p_c - p_t) \qquad 0 < r < R & \text{(A.1)} \\ \dfrac{1}{r}\dfrac{d^2}{dr^2}(rp_t) = -M_t(p_c - p_t) \qquad 0 < r < R & \text{(A.2)} \\ \dfrac{dp_c}{dr}|_{r=0} = \dfrac{dp_t}{dr}|_{r=0} = 0 & \text{(A.3)} \\ p_c|_{r=R} = \bar{p} > 0, \quad p_t|_{r=R} = 0, & \text{(A.4)} \end{cases}$$

where

$$M_c = \frac{\bar{L}_p S}{K_c|\Omega_c|}, \quad M_t = \frac{\bar{L}_p S}{K_t|\Omega_t|}. \tag{A.5}$$

We rewrite the problem (A.1-A.4) in terms of relative pressures and radial coordinate

$$\hat{p}_c = p_c/\bar{p}; \quad \hat{p}_t = p_t/\bar{p}; \quad \hat{r} = r/R, \tag{A.6}$$

thus we obtain:

$$\begin{cases} \dfrac{1}{\hat{r}}\dfrac{d^2}{d\hat{r}^2}(\hat{r}\hat{p}_c) = R^2 M_c(\hat{p}_c - \hat{p}_t) \qquad 0 < \hat{r} < 1 & \text{(A.7)} \\ \dfrac{1}{\hat{r}}\dfrac{d^2}{d\hat{r}^2}(\hat{r}\hat{p}_t) = -R^2 M_t(\hat{p}_c - \hat{p}_t) \qquad 0 < \hat{r} < 1 & \text{(A.8)} \\ \dfrac{d\hat{p}_c}{d\hat{r}}|_{\hat{r}=0} = \dfrac{d\hat{p}_t}{d\hat{r}}|_{\hat{r}=0} = 0 & \text{(A.9)} \\ \hat{p}_c|_{\hat{r}=1} = 1, \quad \hat{p}_t|_{\hat{r}=1} = 0. & \text{(A.10)} \end{cases}$$

We first derive the solution for the relative pressure difference defined as

$$\hat{\psi} = \hat{p}_c - \hat{p}_t, \tag{A.11}$$

so that, subtracting equation (A.8) from equation (A.7) and rearranging boundary conditions, yields the following differential problem for $\hat{\psi}$:

$$\begin{cases} \frac{1}{\hat{r}}\frac{d^2}{d\hat{r}^2}(\hat{r}\hat{\psi}) = \alpha^2\hat{\psi} \qquad 0<\hat{r}<1 & \text{(A.12)} \\ \frac{d\hat{\psi}}{d\hat{r}}|_{\hat{r}=0} = 0 & \text{(A.13)} \\ \hat{\psi}|_{\hat{r}=1} = 1, & \text{(A.14)} \end{cases}$$

where we set

$$\alpha = R\sqrt{M_c + M_t}. \tag{A.15}$$

We set

$$\hat{\psi} = \frac{\varphi}{\hat{r}}, \tag{A.16}$$

so that, substitution of (A.16) into (A.12) yields:

$$\frac{d^2\varphi}{d\hat{r}^2} - \alpha^2\varphi = 0. \tag{A.17}$$

The general solution of the linear second order homogeneous differential equation (A.17) reads:

$$\varphi = \tilde{A}\exp(\alpha\hat{r}) + \tilde{B}\exp(-\alpha\hat{r}), \tag{A.18}$$

and, enforcing (A.16)

$$\hat{\psi} = \frac{\tilde{A}\exp(\alpha\hat{r}) + \tilde{B}\exp(-\alpha\hat{r})}{\hat{r}}, \tag{A.19}$$

where $\tilde{A}$ and $\tilde{B}$ are integration constants to be determined exploiting boundary conditions (A.13-A.14). In order to exploit (A.13) we first compute:

$$\frac{d\hat{\psi}}{d\hat{r}} = \frac{\alpha\hat{r}\tilde{A}\exp(\alpha\hat{r}) - \alpha\hat{r}\tilde{B}\exp(-\alpha\hat{r}) - \tilde{A}\exp(\alpha\hat{r}) - \tilde{B}\exp(-\alpha\hat{r})}{\hat{r}^2}, \tag{A.20}$$

then we observe that

$$\exp(\alpha\hat{r}) = 1 + \alpha\hat{r} + \frac{\alpha^2\hat{r}^2}{2} + O(\alpha^3\hat{r}^3), \tag{A.21}$$

$$\exp(-\alpha\hat{r}) = 1 - \alpha\hat{r} + \frac{\alpha^2\hat{r}^2}{2} + O(\alpha^3\hat{r}^3), \tag{A.22}$$

by means of Taylor expansions around $\alpha\hat{r} = 0$, where, for simplicity of notation, we use the same symbol $O(\alpha^3\hat{r}^3)$ to denote any sum of power series terms which approach 0 faster or equal to $\hat{r}^3$ as $\hat{r} \to 0$. Substituting expansions (A.21-A.22) into (A.20) and rearranging terms yields:

$$\frac{d\hat{\psi}}{d\hat{r}} = \frac{\left(\tilde{A}+\tilde{B}\right)\left(\frac{\alpha^2\hat{r}^2}{2} - 1\right) + O(\alpha^3\hat{r}^3)}{\hat{r}^2} \tag{A.23}$$

Imposing boundary condition (A.13) yields:

$$\frac{d\hat{\psi}}{d\hat{r}}|_{\hat{r}=0} = \lim_{\hat{r}\to 0}\frac{d\hat{\psi}}{d\hat{r}} = 0 \Rightarrow \lim_{\hat{r}\to 0}\frac{\left(\tilde{A}+\tilde{B}\right)\left(\frac{\alpha^2\hat{r}^2}{2} - 1\right) + O(\alpha^3\hat{r}^3)}{\hat{r}^2} = 0, \tag{A.24}$$

which holds if and only if

$$\tilde{B} = -\tilde{A}. \tag{A.25}$$

Starting from (A.19), we can find the solution for $\hat{\psi}$ via (A.25) and exploiting Dirichlet boundary condition (A.14), namely:

$$\hat{\psi}|_{\hat{r}=1} = 1 \Rightarrow \frac{2\tilde{A}\sinh(\alpha\hat{r})}{\hat{r}}|_{\hat{r}=1} = 1 \Rightarrow \tilde{A} = \frac{1}{2\sinh(\alpha)}, \tag{A.26}$$

hence the soultion for the relative pressure difference $\hat{\psi}$ reads:

$$\hat{\psi} = \frac{\sinh(\alpha\hat{r})}{\hat{r}\sinh(\alpha)}. \tag{A.27}$$

We point out that the function $\hat{\psi}$ must be finite in the limit $\hat{r} \to 0$, in fact:

$$\lim_{\hat{r}\to 0} \frac{\sinh(\alpha\hat{r})}{\hat{r}\sinh(\alpha)} = \frac{\alpha}{\sinh(\alpha)} < +\infty. \tag{A.28}$$

In order to compute the complete solution for $\hat{p}_c$ and $\hat{p}_t$, we can rewrite (A.7) and (A.8) as follows:

$$\begin{cases} \dfrac{1}{\hat{r}}\dfrac{d^2}{d\hat{r}^2}(\hat{r}\hat{p}_c) = R^2 M_c \hat{\psi} \qquad 0 < \hat{r} < 1 & \text{(A.29)} \\ \dfrac{d\hat{p}_c}{d\hat{r}}|_{\hat{r}=0} = 0 & \text{(A.30)} \\ \hat{p}_c|_{\hat{r}=1} = 1, & \text{(A.31)} \end{cases}$$

$$\begin{cases} \dfrac{1}{\hat{r}}\dfrac{d^2}{d\hat{r}^2}(\hat{r}\hat{p}_t) = -R^2 M_t \hat{\psi} \qquad 0 < \hat{r} < 1 & \text{(A.32)} \\ \dfrac{d\hat{p}_t}{d\hat{r}}|_{\hat{r}=0} = 0 & \text{(A.33)} \\ \hat{p}_t|_{\hat{r}=1} = 0, & \text{(A.34)} \end{cases}$$

where $\hat{\psi}$ is understood to be the known function given by (A.27), so that the problems (A.29-A.31), (A.32-A.34) are formally decoupled. Setting

$$\hat{p}_c = \frac{\varphi_c}{\hat{r}}; \quad \hat{p}_t = \frac{\varphi_t}{\hat{r}}, \tag{A.35}$$

equations (A.29) and (A.32) reduce to

$$\frac{d^2\varphi_c}{d\hat{r}^2} = R^2 M_c \varphi, \tag{A.36}$$

$$\frac{d^2\varphi_t}{d\hat{r}^2} = -R^2 M_t \varphi, \tag{A.37}$$

and the general solutions read

$$\varphi_c = \frac{R^2 M_c}{\alpha^2}\varphi + \tilde{C}\hat{r} + \tilde{D}, \tag{A.38}$$

$$\varphi_t = -\frac{R^2 M_t}{\alpha^2}\varphi + \tilde{E}\hat{r} + \tilde{F}, \tag{A.39}$$

and, exploiting (A.16), (A.35)

$$\hat{p}_c = \frac{R^2 M_c}{\alpha^2}\hat{\psi} + \tilde{C} + \frac{\tilde{D}}{\hat{r}}, \tag{A.40}$$

$$\hat{p}_t = -\frac{R^2 M_t}{\alpha^2}\hat{\psi} + \tilde{E} + \frac{\tilde{F}}{\hat{r}}, \tag{A.41}$$

where $\tilde{C}$, $\tilde{D}$, $\tilde{E}$, $\tilde{F}$ are integration constants to be determined exploiting the proper boundary conditions for $\hat{p}_c$ and $\hat{p}_t$. We impose that $\hat{p}_c$ and $\hat{p}_t$ are finite in the limit $\hat{r} \to 0$ i.e, since (A.28) holds for $\hat{\psi}$:

$$\tilde{D} = \tilde{F} = 0. \tag{A.42}$$

Furthermore, when accounting for (A.42) and (A.24) in (A.40-A.41), $\hat{p}_c$ and $\hat{p}_t$ automatically satisfy the Neumann boundary conditions (A.30) and (A.33), respcetively. Exploiting the Dirichlet boundary conditions (A.31-A.34) we can find $\tilde{C}$ and $\tilde{E}$, namely:

$$\hat{p}_c|_{\hat{r}=1} = 1 \Rightarrow \tilde{C} = 1 - \frac{R^2 M_c}{\alpha^2}; \quad \hat{p}_t|_{\hat{r}=1} = 0 \Rightarrow \tilde{E} = \frac{R^2 M_t}{\alpha^2}. \tag{A.43}$$

Enforcing definition (A.15) in (A.43) we deduce:

$$\tilde{C} = \tilde{E}, \tag{A.44}$$

so that the solutions for $\hat{p}_c$ and $\hat{p}_t$ rewrite:

$$\hat{p}_c = \frac{R^2 M_c}{\alpha^2}\hat{\psi} + \frac{R^2 M_t}{\alpha^2}, \tag{A.45}$$

$$\hat{p}_t = -\frac{R^2 M_t}{\alpha^2}\hat{\psi} + \frac{R^2 M_t}{\alpha^2}, \tag{A.46}$$

respectively. We check that the solutions given by (A.45-A.46) satisfy (A.11), namely

$$\hat{p}_c - \hat{p}_t = \frac{R^2 M_c}{\alpha^2}\hat{\psi} + \frac{R^2 M_t}{\alpha^2} + \frac{R^2 M_t}{\alpha^2}\hat{\psi} - \frac{R^2 M_t}{\alpha^2} = \hat{\psi}, \tag{A.47}$$

where we enforced definition (A.15).

We finally explicitly state the solution of the coupled problem (A.7-A.10) by means of (A.27) and rearranging terms:

$$\hat{p}_c = \frac{1}{M_c + M_t}\left(M_t + \frac{M_c \sinh(\alpha\hat{r})}{\hat{r}\sinh(\alpha)}\right), \tag{A.48}$$

$$\hat{p}_t = \frac{M_t}{M_c + M_t}\left(1 - \frac{\sinh(\alpha\hat{r})}{\hat{r}\sinh(\alpha)}\right). \tag{A.49}$$

## References


Alarcón, T., Byrne, H.M., Maini, P.K., 2003. A cellular automaton model for tumour growth in inhomogeneous environment. Journal of Theoretical Biology 225, 257–274.

Ambrosi, D., Gamba, A., Serini, G., 2004. Cell directionality and chemotaxis in vascular morphogenesis. Bulletin of mathematical biology 66, 1851–1873.

Asaishi, K., Endrich, B., Götz, A., Messmer, K., 1981. Quantitative analysis of microvascular structure and function in the amelanotic melanoma a-mel-3. Cancer research 41, 1898–1904.

Batchelor, G.K., 2000. An introduction to fluid dynamics. Cambridge university press.

Beavers, G.S., Joseph, D.D., 1967. Boundary conditions at a naturally permeable wall. Journal of Fluid Mechanics 30, 197–207.

Boucher, Y., Baxter, L.T., Jain, R.K., 1990. Interstitial pressure gradiennts in tissue-isolated and subcutaneous tumors: implications for therapy. Cancer Research 50, 4478–4484.

Boucher, Y., Brekken, C., Netti, P., Baxter, L., Jain, R., 1998. Intratumoral infusion of fluid: estimation of hydraulic conductivity and implications for the delivery of therapeutic agents. British journal of cancer 78, 1442.

Burridge, R., Keller, J., 1981. Poroelasticity equations derived from microstructure. Journal of acoustical society of America 70, 1140–1146.

Carman, P., 1937. Fluid flow through granular beds. Transactions-Institution of Chemical Engineeres 15, 150–166.

Davit, Y., Bell, C., Byrne, H., Chapman, L., Kimpton, L., Lang, G., Leonard, K., Oliver, J., Pearson, N., Shipley, R., Waters, S., Whiteley, J., Wood, B., Quintard, M., 2013. Homogenization via formal multiscale asymptotics and volume averaging: how do the two techniques compare? Advances in Water Resources 62, 178–206.

Di Federico, V., Cintoli, S., Bizzarri, G., 2002. Moto alla stokes in condotti a sezione variabile. 28 Convegno di Idraulica e Costruzioni idrauliche Potenza 16-19 settembre 2002 .

Fahareus, R., Lindqvist, T., 1931. The viscosity of the blood in narrow capillary tubes. American Journal of Physiology 96, 562–568.

Hahnfeldt, P., Panigrahy, D., Folkman, J., Hlatky, L., 1999. Tumor development under angiogenic signaling a dynamical theory of tumor growth, treatment response, and postvascular dormancy. Cancer research 59, 4770–4775.

Hashizume, H., 2000. Openings between defective endothelial cells explain tumor vessel leakiness. Am. J. Pathol. 156, 1363–1380.

Heijs, A.W.J., Lowe, C.P., 1995. Numerical evaluation of the permeability and the kozeny constant for two types of porous media. Phys. Rev. E 51, 4346–4352. doi:10.1103/PhysRevE.51.4346.

Holmes, M., 1995. Introduction to perturbation method. Springer-Verlag.

Jain, R.K., 1987. Transport of molecules in the tumor interstitium: a review. Cancer Research 47, 3039–3051.

Jain, R.K., Baxter, L.T., 1988. Mechanisms of heterogeneous distribution of monoclonal antibodies and other macromolecules in tumors: significance of elevated interstitial pressure. Cancer Research 48, 7022–7032.

Jain, R.K., Tong, R.T., Munn, L.L., 2007. Effect of vascular normalization by antiangiogenic therapy on interstitial hypertension, peritumor edema, and lymphatic metastasis: insights from a mathematical model. Cancer Res 67, 2729–2735.

Jones, I.P., 1973. Low reynolds number flow past a porous spherical shell. Mathematical Proceedings of the Cambridge Phylosofical Society 73, 231–238.

Kitanidis, P.K., Dykaar, B.B., 1997. Stokes flow in a slowly varying two-dimensional periodic pore. Transport in porous media 26, 89–98.

Kozeny, J., 1927. Ueber kapillare leitung des wassers im boden. Sitzungsber. Akad. Wiss. Wien 136, 271–306.

Malevich, A., Mityushev, V., Adler, P., 2006. Stokes flow through a channel with wavy walls. Acta mechanica 182, 151–182.

Matyka, M., Khalili, A., Koza, Z., 2008. Tortuosity-porosity relation in porous media flow. Phys. Rev. E 78, 026306. doi:10.1103/PhysRevE.78.026306.

Matzavinos, A., Kao, C.Y., Green, J.E.F., Sutradhar, A., Miller, M., Friedman, A., 2009. Modeling oxygen transport in surgical tissue transfer. Proceedings of the National Academy of Sciences 106, 12091–12096.

Mei, C.C., Vernescu, B., 2010. Homogenization Methods for multiscale mechanics. World Scientific.

Modok, S., Hyde, P., Mellor, H., Roose, T., Callaghan, R., 2006. Diffusivity and distribution of vinblastine in three-dimensional tumour tissue: Experimental and mathematical modelling. European Journal of Cancer 42, 2404–2413.

Modok, S., Scott, R., Alderden, R., Hall, M., Mellor, H., Bohic, S., Roose, T., Hambley, T., Callaghan, R., 2007. Transport kinetics of four-and six-coordinate platinum compounds in the multicell layer tumour model. British Journal of Cancer 97, 194–200.

Owen, M.R., Alarcon, T., Maini, P.K., Byrne, H.M., 2008. Angiogenesis and vascular remodelling in normal and cancerous tissues. Journal of Mathematical Biology 58, 689–721.

Penta, R., Ambrosi, D., Quarteroni, A., 2014a. Multiscale homogenization for fluid and drug transport in vascularized malignant tissues. Mathematical Models and Methods in Applied Sciences (M3AS) doi:10.1142/S0218202515500037.

Penta, R., Ambrosi, D., Shipley, R.J., 2014b. Effective governing equations for poroelastic growing media. The Quarterly Journal of Mechanics and Applied Mathematics 67, 69–91.

Powathil, G.G., Gordon, K.E., Hill, L.A., Chaplain, M.A., 2012. Modelling the effects of cell-cycle heterogeneity on the response of a solid tumour to chemotherapy: biological insights from a hybrid multiscale cellular automaton model. Journal of theoretical biology 308, 1–19.

Pries, A.R., Secomb, T.W., Gaehtgens, P., Gross, J.F., 1990. Blood flow in microvascular networks. experiments and simulations. Circulation Research 67, 826–834.

Pries, A.R., Secomb, T.W., Gaethgens, P., 1998. Structural adaptation and stability of microvascular networks: theory and simulations. American Journal of physiology 275, 349–360.

Rand, P.W., Lacombe, E., Hunt, H.E., 1964. Viscosity of normal human blood under normothermic and hypothermic conditions. Journal of Applied Physiology 19, 117–122.

Sanchez-Palencia, E., 1983. Homogenization method for the study of composite media. Asymptotic analysis II-Lecture notes in mathematics 985, 192–214.

Sevick, E.M., Jain, R.K., 1991. Measurement of capillary filtration coefficient in a solid tumor. Cancer research 51, 1352–1355.

Shipley, R., 2008. Multiscale Modelling of Fluid and Drug Transport in Vascular Tumors. Ph.D. thesis. St. Hugh's College University of Oxford.

Shipley, R.J., Chapman, J., 2010. Multiscale modelling of fluid and drug transport in vascular tumors. Bulletin of Mathematical Biology. 72, 1464–1491.

Swabb, E.A., Wei, J., Gullino, P.M., 1974. Diffusion and convection in normal and neoplastic tissues. Cancer Research 34, 2814–2822.

Taffetani, M., de Falco, C., Penta, R., Ambrosi, D., Ciarletta, P., 2014. Biomechanical modelling in nanomedicine: multiscale approaches and future challenges. Archive of Applied Mechanics doi:10.1007/s00419-014-0864-8.

Yoshii, Y., Sugiyama, K., 1988. Intercapillary distance in the proliferating area of human glioma. Cancer research 48, 2938–2941.

# MOX Technical Reports, last issues

**Dipartimento di Matematica "F. Brioschi",**
**Politecnico di Milano, Via Bonardi 9 - 20133 Milano (Italy)**

**44/2014** Pezzuto, s.; Ambrosi,D.
*Active contraction of the cardiac ventricle and distortion of the microstructural architecture*

**45/2014** Pezzuto, s.; Ambrosi,D.; Quarteroni, A.
*An orthotropic active-strain model for the myocardium mechanics and its numerical approximation*

**46/2014** Penta, R; Ambrosi, D.
*The role of the microvascular tortuosity in tumor transport phenomena*

**43/2014** Brugiapaglia, S.; Micheletti, S.; Perotto, S.
*Compressed solving: a numerical approximation technique for PDEs based on compressed sensing*

**42/2014** Canale, A.; Vantini, S.
*Constrained Functional Time Series: an Application to Demand and Supply Curves in the Italian Natural Gas Balancing Platform*

**41/2014** Esfandiar, B.; Porta, G.; Perotto, S.; Guadagnini, A.
*Impact of space-time mesh adaptation on solute transport modeling in porous media*

**40/2014** Antonietti, P.F.; Mazzieri, I.; Quarteroni, A.
*Improving seismic risk protection through mathematical modeling*

**39/2014** Ghiglietti, A.; Paganoni, A.M.
*Statistical inference for functional data based on a generalization of Mahalanobis distance*

**38/2014** Shen, H.; Truong, Y.; Zanini, P.
*Independent Component Analysis for Spatial Stochastic Processes on a Lattice*

**37/2014** Giuliani, N.; Mola, A.; Heltai, L.; Formaggia,L.
*FEM SUPG stabilisation of mixed isoparametric BEMs: application to linearised free surface flows*